Monthly Notices
of the
ROYAL ASTRONOMICAL SOCIETY

MNRAS **473,** 3671–3692 (2018) doi:10.1093/mnras/stx2560

First Extended Catalogue of Galactic bubble infrared fluxes from *WISE* and *Herschel*⋆ surveys

F. Bufano,[1]† P. Leto,[1] D. Carey,[2] G. Umana,[1] C. Buemi,[1] A. Ingallinera,[1] A. Bulpitt,[2] F. Cavallaro,[1,3,4] S. Riggi,[1] C. Trigilio[1] and S. Molinari[5]

[1]*INAF-Osservatorio Astrofisico di Catania, Via Santa Sofia 78, I-95123 Catania, Italy*
[2]*School of Computing, University of Leeds, E C Stoner Building, Leeds, LS2 9JT*
[3]*Università di Catania, Dipartimento di Fisica e Astronomia, Via Santa Sofia, 64, I-95123 Catania, Italy*
[4]*CSIRO Astronomy and Space Science, PO Box 76, Epping, NSW 1710, Australia*
[5]*INAF-Istituto di Astrofisica e Planetologia Spaziale, Via Fosso del Cavaliere 100, I-00133 Roma, Italy*

Accepted 2017 September 29. Received 2017 September 25; in original form 2016 August 4

ABSTRACT

In this paper, we present the first extended catalogue of far-infrared fluxes of Galactic bubbles. Fluxes were estimated for 1814 bubbles, defined here as the 'golden sample', and were selected from the Milky Way Project First Data Release (Simpson et al.) The golden sample was comprised of bubbles identified within the *Wide-field Infrared Survey Explorer* (*WISE*) dataset (using 12- and 22-μm images) and *Herschel* data (using 70-, 160-, 250-, 350- and 500-μm wavelength images). Flux estimation was achieved initially via classical aperture photometry and then by an alternative image analysis algorithm that used active contours. The accuracy of the two methods was tested by comparing the estimated fluxes for a sample of bubbles, made up of 126 H II regions and 43 planetary nebulae, which were identified by Anderson et al. The results of this paper demonstrate that a good agreement between the two was found. This is by far the largest and most homogeneous catalogue of infrared fluxes measured for Galactic bubbles and it is a step towards the fully automated analysis of astronomical datasets.

Key words: methods: data analysis – techniques: image processing – techniques: photometric – catalogues – ISM: bubbles – infrared: ISM.

1 INTRODUCTION

Bubbles are one of the most intriguing objects found within recent large-scale infrared (IR) surveys (e.g. Churchwell et al. 2006; Mizuno et al. 2010; Wachter et al. 2010; Simpson et al. 2012). The term 'bubbles' is used to classify diffuse emissions with a ring, disc or shell-like shape distributed throughout the entire Galactic plane, although they can be the result of different astrophysical phenomena. For example, some are related to young H II regions, and thus to hot massive stars that mould the interstellar medium (ISM), and others are related to circumstellar envelopes that surround stars at later evolutionary stages, such as planetary nebulae (PNe), luminous blue variables (LBVs), supernova remnants (SNRs), etc.

Studies of bubbles enable us to derive the structural and physical properties of these objects. For instance, such work uncovers important information about their central objects, the stellar winds they arise from and the environment in which they expand.

Churchwell et al. (2006, 2007) have catalogued almost 600 bubbles (typically a few arcmin wide), listing the most prominent ones detected in the images from the *Spitzer* Galactic Legacy Infrared Mid-Plane Survey Extraordinaire (GLIMPSE; Benjamin et al. 2003). GLIMPSE surveyed the Galactic plane between sky regions found at $|b| \leq 1°$–$2°$ and $|l| \leq 65°$ using four different IR wavebands (3.6, 4.5, 5.8 and 8 μm). Based on the spatial coincidence with known H II regions, Churchwell et al. (2007) claimed that many of the IR bubbles are produced by O and early-B stars. The emission observed with the 8-μm band, in general associated with photo-dissociated regions (PDRs), is mainly due to polycyclic aromatic hydrocarbon (PAH) molecules. These emit via fluorescence at 7.7 and 8.6 μm (Tielens 2008), when excited by the far-ultraviolet photons from the hot central star. PAH emission at 8 μm from bubbles associated with H II regions is strong, while in PNe, for example, it is moderately strong or weak/absent if it comes from C-rich or O-rich PNe, respectively (Volk & Kwok 2003; Anderson et al. 2012).

However, when analysing images from the *Spitzer*/Multiband Imaging Photometer for *Spitzer* Inner Galactic Plane (MIPSGAL; Carey et al. 2009), Deharveng et al. (2010) noticed that the emission at 24 μm of bubbles from Churchwell et al. (2006) is frequently observed inside the bubble with a morphology that closely traces the

⋆ *Herschel* is an ESA space observatory with science instruments provided by European-led Principal Investigator consortia and with important participation from NASA.

† E-mail: milena.bufano@gmail.com

© 2017 The Authors
Published by Oxford University Press on behalf of the Royal Astronomical Society

Downloaded from https://academic.oup.com/mnras/article-abstract/473/3/3671/4633601
by guest
on 13 March 2018

radio continuum emission at 20 cm from ionized gas. They claimed that the emission at this wavelength is dominated by hot thermal dust, containing a contribution from very small grains (probably silicates) that are out of thermal equilibrium. Mizuno et al. (2010) inspected 24-μm MIPSGAL images, looking for circularly symmetric and extended emissions. They found a total of 416 bubbles, typically smaller than those identified by Churchwell et al. (2006) ($\lesssim$1 arcmin). A fraction of the sample ($\sim$16 per cent) was already identified in previous works, and almost all of them were classified as PNe, LBVs or SNRs, leading the authors to conclude, based also on a strong morphological similarity, that their catalogue included primarily evolved stars.

Nowadays, information from existing IR surveys can help to improve knowledge of the bubble structures and their origins in two ways. First, a larger area of the Milky Way has been covered, which has increased the number of known objects. Secondly, bubbles have been observed in different wavebands. With this purpose, we analysed: (i) the available data from the *Wide-field Infrared Survey Explorer* (*WISE*), which mapped the entire sky in four IR bands, in particular at 12 and 22 μm, resembling the 8- and 24-μm bands from *Spitzer* GLIMPSE and MIPSGAL, although with a lower resolution; (ii) the data from the *Herschel* infrared Galactic Plane Survey (Hi-GAL; Molinari et al. 2010), which covers the entire Galactic plane ($|b| \leq 1^\circ$) at longer wavelengths than *WISE* tracing, for example, the distribution of the cold dust (see Section 3).

Despite the richness of information available, only a few works have exploited such IR data for the bubble studies. Anderson et al. (2012, hereafter A12) analysed a sample of bubbles including 126 H II regions and 43 known PNe, with the aim of discriminating between the two types of sources based on their IR colours. Paladini et al. (2012) published a study on 16 known H II regions in order to understand the mechanisms regulating massive star formation. Both published IR flux catalogues limited to the studied bubbles, where fluxes were estimated by 'interactive' methods. Indeed, in these analyses, the dimensions of the bubble, and thus the radius used for the flux estimation, were visually adjusted and chosen on a case-by-case basis.

In an era of big data, using only this kind of approach would be simply anachronistic when considering the huge flow of information produced by the incoming unbiased surveys that will be carried out, for example, at the Large Synoptic Survey Telescope (LSST), the *James Webb Space Telescope* (*JWST*) and the Square Kilometer Array (SKA).

In this paper, we present two methods for the automated measurement of bubble fluxes and, as a final product, a catalogue with the emitted IR fluxes – estimated using these methods – of a sample of 1814 Galactic bubbles. The paper is organized as follows. In Section 2, we present the selected bubble sample (whose measured fluxes are published in the final catalogue). In Section 3, we give a description of the technical characteristics of the employed IR surveys. In Section 4, we describe the methods used for the flux measurements. In Section 5, we present the structure of the published catalogue. Finally, we discuss the results in Section 6 and we conclude in Section 7.

2 BUBBLE SAMPLE SELECTION

We consider the Galactic bubble catalogue produced by Simpson et al. (2012) as a database of confirmed bubbles. The catalogue consists of 5106 bubbles that have been identified by citizen scientists via visual inspection of the GLIMPSE and MIPSGAL infrared images, acquired at 8 and 24 μm, respectively.[1] This dataset was created by volunteers marking regions of images where bubbles are located. They drew a circular annulus around bubble features and this was scaled in size and stretched into an elliptical annulus resembling the prominent features of bubbles. The identified bubbles have been further split into two groups: 3744 *large* bubbles, drawn by users as ellipses, and 1362 *small* bubbles, which were too small to be drawn around in detail but can be still identified. The catalogue lists the centroid position and radius for each bubble, averaged over at least five individual users drawings (see Section 3.1 in Simpson et al. 2012 for details). For *large* bubbles, the catalogue also reports parameters such as the inner major and minor axes, outer major diameter, eccentricity and position angle, while the effective radius and thickness values are calculated from geometric means of such diameters (as given in equation 1 by Simpson et al. 2012). In particular, as the bubbles were identified on GLIMPSE and MIPSGAL images, they are distributed exclusively over the inner Galactic plane ($|l| \leq 65^\circ$).

As a first step, we selected only those bubbles located in fields observed by the Hi-GAL survey, obtaining a sample of 4988 bubbles over the original 5106, due to the fact that Hi-GAL covers the Galactic latitudes $|b| \leq 1^\circ$ at all Galactic longitudes while *Spitzer* extends at least up to $|b| = 2^\circ$ towards the Galactic Centre region.

At the same time, we found that a large number of bubbles were projected over each other and therefore could contaminate the final flux estimation. Thus, we decided to clean the sample and create a *golden sample*. First, we defined a circular region centred on each bubble centroid and with a radius equal to the outer diameter or to the radius given by Simpson et al. (2012) in the case of a *large* or a *small* bubble, respectively. Then we selected those bubbles whose circular region is not overlapping with that of any other bubble. We added an extra constraint for the cases where a *small* bubble was overlapping a *large* bubble. Indeed, having taken for *large* bubbles a radius equal to the outer diameter in order to guarantee including the totality of the emission at the different wavelength ranges, we risk removing *small* bubbles at their very border that are not contaminated. Therefore, if the distance between the two centroids was larger than the smallest of the two radii (corresponding in most cases to the *small*-bubble radius), then both bubbles were kept separated and included in the golden sample. In addition, this enabled the removal of duplications of single bubbles that were present in both catalogues. The selected final sample consisted of a total of 1814 bubbles: 45 per cent of the *small* bubbles from Simpson et al. (2012) were kept, whilst 33 per cent of the *large* bubbles. Nonetheless, the *large* bubbles still represent two-thirds of the golden sample. A catalogue of this sample has been produced, listing for each bubble the relative Galactic coordinates (corresponding to their centroids) and their radius ($R_{\rm cat}$), which is either equal to the bubble's effective radius for *small* bubbles or to half the outer diameter for *large* bubbles.

3 DATA DESCRIPTION

The images from which we estimated the fluxes emitted by the bubbles of the golden sample are taken from the *WISE* and Hi-GAL surveys.

[1] See http://www.milkywayproject.org.

Downloaded from https://academic.oup.com/mnras/article-abstract/473/3/3671/4633601
by guest
on 13 March 2018

3.1 *WISE* image database

WISE (Wright et al. 2010) was a mission that mapped the entire sky in four IR bands: 3.4, 4.6, 12 and 22 μm (data used here are from the 2012 March 14 release).

In this work, we used the 12- and 22-μm bands, as these trace similar dust components as the GLIMPSE 8-μm and MIPSGAL 24-μm bands, respectively. However, the 12-μm bandpass is significantly broader than GLIMPSE's 8.0-μm, collecting emissions from PAH features at 11.2, 12.7 and 16.4 μm (Tielens 2008). The PAH features at 7.7 and 8.6 μm also fall within the bandpass although at diminished sensitivity. The spatial resolutions in the two bands are 6.5 and 12 arcsec and the sensitivities are 1 mJy and 6 mJy, respectively. The *WISE* image data have units of DN, thus we used a DN- to-Jy conversion factor equal to 1.8326×10^{-6} and 5.2269×10^{-5} for the 12- and 22-μm bands, respectively (see the *WISE* explanatory supplement[2]).

3.2 *Herschel* image database

The Hi-GAL survey was performed using the Photoconductor Array Camera and Spectrometer (PACS; Poglitsch et al. 2010) and the Spectral and Photometric Imaging Receiver (SPIRE; Griffin et al. 2010) instruments onboard the *Herschel* Space Observatory (Pilbratt et al. 2010). Hi-GAL maps the Galactic plane ($0^\circ \leq l \leq 360^\circ$, $|b| \leq 1^\circ$) in five wavebands, namely 70, 160, 250, 350 and 500 μm, providing a well-sampled coverage of the frequency range where the spectral energy distribution (SED) of cold dust peaks. The spatial resolutions of these images are 6.7, 11, 18, 25 and 37 arcsec, respectively. Images were reduced using the ROMAGAL data-processing code, for both PACS and SPIRE data; see Traficante et al. (2011) and Molinari et al. (2016) for details.

4 BUBBLE FLUX MEASUREMENTS

We estimated the flux coming from each of the 1814 bubbles belonging to the golden sample using two different methods: the first method is classical aperture photometry, in which we measured the flux within a circular area centred on the source; the second method uses the same aperture but selects the flux coming from the bubble using a segmentation mask, which removes any pixel coming from nearby contaminating sources and from the background. Before applying such methods, we prepared our sample images, as described in the following subsection.

4.1 Dataset preparation

Using the selected golden sample catalogue, sources were cut out of the *WISE* and *Herschel* image datasets using a bounding box that was centred on the bubbles' centroid and whose width was equal to 10 times $R_{\rm cat}$. Each map (cut out) was projected on to the N–E equatorial direction and scaled to the pixel scale of a reference image using the MONTAGE toolkit.[3] The image taken as reference was the image with the smallest pixel scale, that is, the *WISE* image at 12 μm (1.37 arcsec pix^{-1}). This allowed seven images to be produced for each source with an identical pixel grid.

[2] http://wise2.ipac.caltech.edu/docs/release/allsky/expsup/sec2_3f.html
[3] http://montage.ipac.caltech.edu/

4.2 Photometric methods

4.2.1 Aperture photometry

We estimated the flux coming from each source in different bands measuring the flux falling into a circular area centred on the bubble centroid coordinates given by Simpson et al. (2012), with a radius ($R_{\rm ph}$) chosen equal to

$$R_{\rm ph} = \sqrt{(2R_{\rm cat})^2 + ({\rm FWHM})^2}, \quad (1)$$

where FWHM is the beam size for each bandpass. The local background level has been estimated just outside the aperture, over an annular area between $R_{\rm ph}$ and $2R_{\rm ph}$ and it is equal to the sigma-clipped mean (2σ level). This was chosen to remove very bright compact objects or spurious spikes. The average background level was then subtracted from each pixel value within the source aperture, before computing the total aperture flux of the bubble.

4.2.2 Segmentation photometry

This method made use of a 'segmentation mask' to select the flux coming from each bubble. In image processing, segmentation is the process of partitioning of a digital image into its component parts and it was used here to define bubble regions. To enable the segmentation of bubbles, a localized active contours algorithm (Lankton & Tannenbaum 2009) was used, which also incorporated gradient information via magnetostatic forces (Xie & Mirmehdi 2008). In our paper's approach, many of the difficulties associated with the use of localized contours were overcome by adaptively selecting the appropriate kernel sizes that are required by this algorithm (further details in Appendix A). In other words, this paper's active contour algorithm finds bright objects that have large gradients. In images where there are many high gradient regions, the contour could grow wildly around the image, at least without human intervention, which is not feasible in this case. This was the case for *Herschel* images acquired at $\geq$160 μm as they had high background contamination. The same is true for *WISE* images at 12 μm as they contained numerous compact field objects. Thus, we decided to optimize the method on the 70-μm images, as bubble contours at this band generally include those at shorter wavelengths and, at the same time, trace dust distribution better than at longer wavelengths.

Thus, segmentation masks have been obtained from original *Herschel* 70-μm images, and consequently they have the same pixel scale. Because bubble images were resampled to the *WISE* 12-μm pixel scale (as described in Section 4.1), we also performed the resampling of the segmentation mask in order to make them match. Moreover, to take into account the instrumental effect on the bubble contours in images at lower resolution than 70 μm, we convolved the mask with a Gaussian profile to correct the beam size differences, before applying it to the corresponding image. This smoothed the mask borders and mimicked the instrumental effect, assigning a fractional value between 0 and 1 to each pixel, which was finally replaced with 1, to produce the new mask.

By using the segmentation map, we mask anything that falls in the aperture $R_{\rm ph}$ but is not expected to be part of the bubble. Any other bright segmented source falling in the background annulus was also removed, before we estimated the average background level value. As a consequence, we used a shallower clipping level (3σ) than in the aperture method. The average background level has been subtracted from each pixel value in the aperture region masked as the bubble, and then summed to estimate the flux of the bubble ('segmentation' flux). Comparing the background average

Downloaded from https://academic.oup.com/mnras/article-abstract/473/3/3671/4633601
by guest
on 13 March 2018

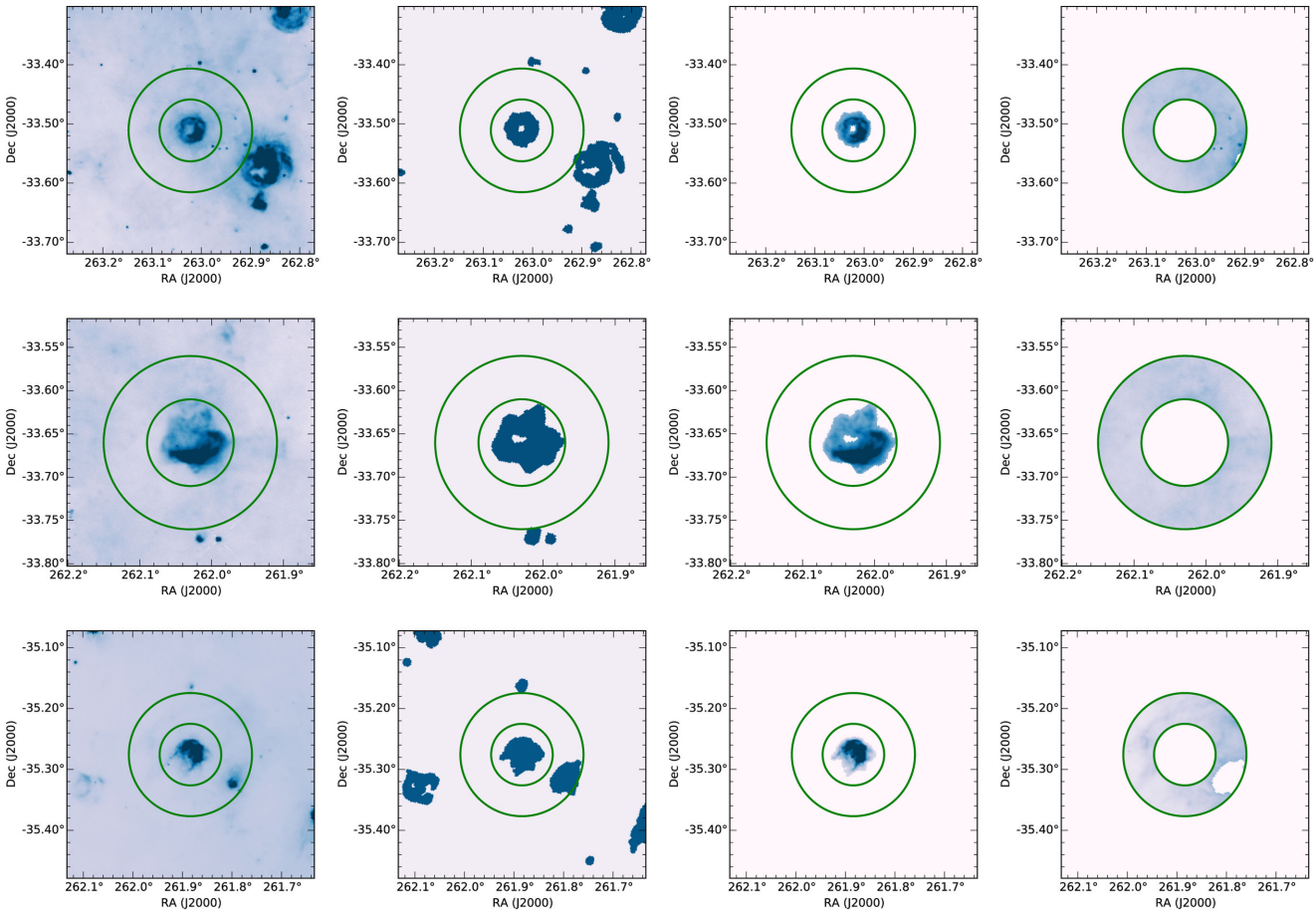

Figure 1. Examples of the application of the two photometric methods on different bubbles: 1G354588+000038 (first row), 1G354008+006116 (second row) and 1G352598–001860 (third row). *Herschel* images at 70 μm have been shown for all the bubbles, and aperture and background regions of radius $R_{\rm ph}$ and $R_{\rm bkg}$, respectively, shown by green circles. The first column shows the bubble fields, the second column shows the segmentation mask produced for the specific field and the third and fourth columns show the aperture and background regions, respectively, obtained using such a mask, as described in Section 4.

level estimated in this way with that of the aperture photometry, we found that they are in agreement within 5 per cent for 85 per cent of the bubbles. The aperture background level turned out to be higher than the segmentation one in around 8 per cent of the cases, most frequently when the presence of extended emission in the background region increased the background sigma value and thus made the sigma-clipping less effective. In other cases (around 7 per cent), the segmentation did not work correctly in masking bright nearby sources, causing a higher average background level.

Examples of the application of the two photometric methods are shown in Fig. 1. We did not provide flux measurements at a given wavelength for those bubbles that exceed 10 per cent of saturated pixels within $R_{\rm ph}$, as with such a high fraction of 'NaN' values the bubble flux estimate would not be reliable. In any case, they represent a very small fraction of the total sample: 24/1814 for *WISE* images; 4/1814 within *Herschel* images acquired at 250 and 500 μm; and 2/1814 for *Herschel* images taken at 350 μm.

For both methods, the uncertainty on the flux is calculated as the sum in quadrature of the background and source counts error over the total number (N) of pixels within $R_{\rm ph}$ over which the flux was calculated. The source counts error is equal to the photon noise in the case of *WISE* images, or to the calibration uncertainties for the *Herschel* maps due to the uncertainties in the theoretical models of the SED of the calibrators and equal to 5 per cent of the flux for PACS images (Balog et al. 2014) and to 4 per cent for those from SPIRE (Bendo et al. 2013). The background error is given by the sum in quadrature of the photon noise/calibration error within the background annulus and the background standard deviation.

Additionally, along with the measured total flux and the relative uncertainty, we provide a value, reported as the signal-to-noise ratio (S/N), which corresponds to the ratio between the median of the background subtracted pixel values within $R_{\rm ph}$ and the background standard deviation. Such values can be used as an indicator of the significance of the detection with respect to the background level.

Finally, we assumed that the contamination from bright compact sources falling in the aperture is negligible, based on the results of previous work (i.e. A12) and of a statistical analysis conducted on this paper's data. A12 found that as H II regions are in general much brighter than any point source within the aperture, the removal of such point sources has a minimal impact on the derived fluxes. In the same way, for less extended bubbles, such as PNe, the small characteristic angular size makes it unlikely that there is a spatial coincidence with point sources. Thus, there is likely to be no consequent contamination of the bubble flux. The possible contribution by compact objects to the bubble flux measured in this paper was also checked. Assuming that compact objects are mainly stars, we estimated their flux contribution at 12 μm, considering that the stellar SED is usually the strongest at this wavelength, relative to

Downloaded from https://academic.oup.com/mnras/article-abstract/473/3/3671/4633601
by guest
on 13 March 2018

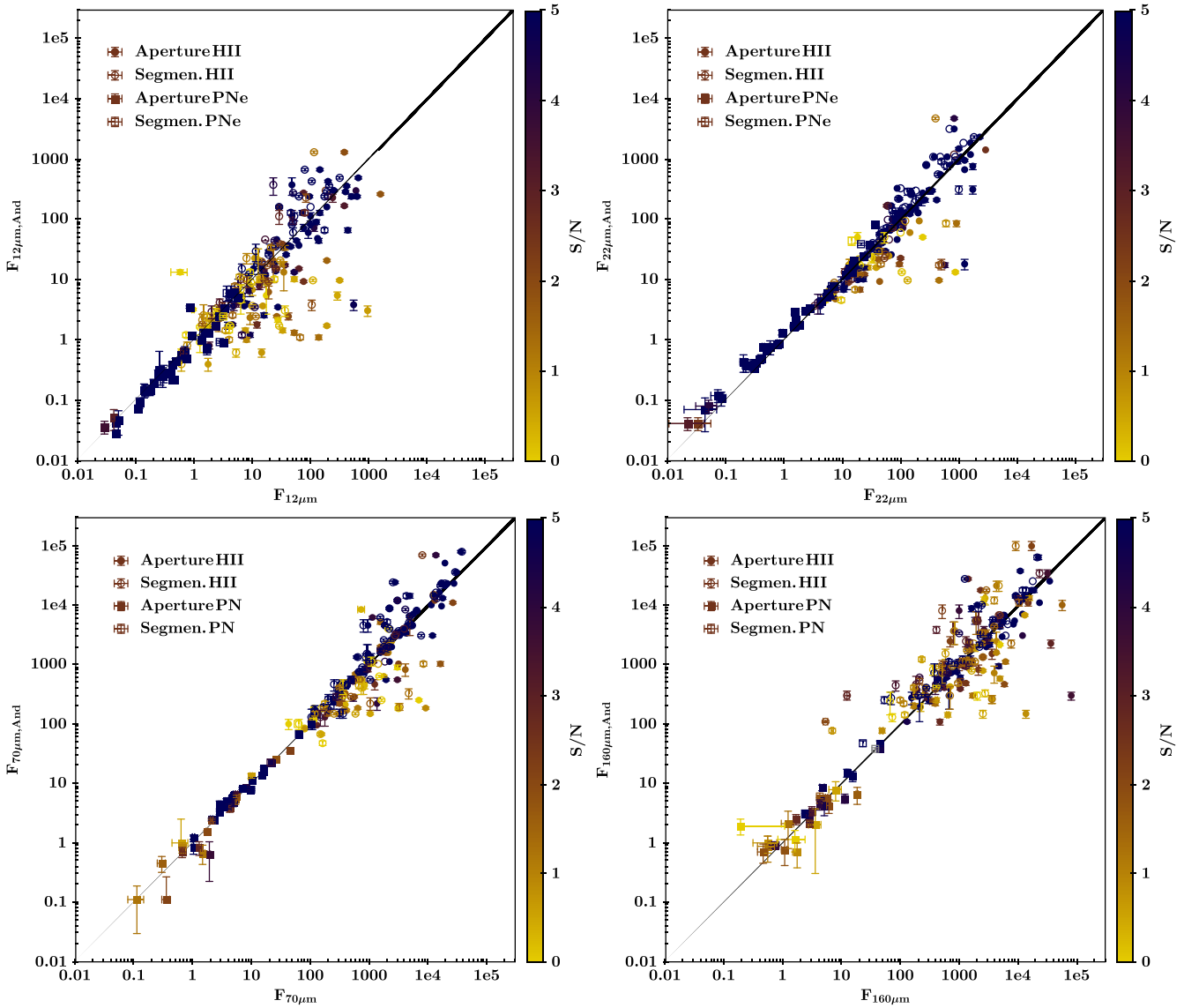

Figure 2. Comparison between photometry obtained with our automated methods and the results of A12. Fluxes from H II regions and PNe are displayed with circles and squares, respectively. For aperture photometry, filled dots are used, while dots for the segmentation photometry are empty. Fluxes are given in Jy. The colour scale indicates the S/N characteristic of each of our measurements.

others used in this paper. From the AllWISE Source Catalogue,[4] we selected the compact objects consistent with a single point spread function and with no saturated pixels, located in the same sky region of the golden sample bubbles. We cross-matched the two catalogues and found the number of compact objects included in the aperture radius of each bubble, calculating their total flux and contribution to the bubble aperture flux. We found that for *large* bubbles the fraction of bubbles with a flux contamination higher than 10 per cent is around 25 per cent (298/1181), while for *small* bubbles it is around 15 per cent. This confirms the marginal contribution of compact objects to the bubbles' flux measured already at 12 μm, which is expected to be the band most affected by contaminants. It is worth stressing that 3 per cent of the *small* bubbles have a contamination higher than 50 per cent, most likely due to the coincidence of the compact object with the bubble itself. Most importantly, no compact objects are included in the aperture radii of one-third of the *small* bubbles.

[4] http://irsa.ipac.caltech.edu/cgi-bin/Gator/nph-scan?submit=Select&projshort=WISE

4.3 Comparison with Anderson et al. (2012)

Recently, A12 analysed the distribution of far-IR emissions from H II regions and PNe in order to find a criterion to discriminate these objects simply using their IR colours. They collected a sample of 43 PNe and 126 H II regions. In order to test their diagnostic method, H II regions have been carefully chosen to span a wide range of angular sizes ($1.1 \leq R \leq 25.9$ arcmin). In particular, they include small-size H II regions (i.e. young compact H II regions in early evolutionary stages or more evolved H II regions at extreme distances from the observer), as these can be easily mistaken for typical PNe, having similar dimensions. The sample of objects presented, both H II regions and PNe, is numerically limited but it is composed of bright examples of these classes, and thus they are relatively

Downloaded from https://academic.oup.com/mnras/article-abstract/473/3/3671/4633601
by guest
on 13 March 2018

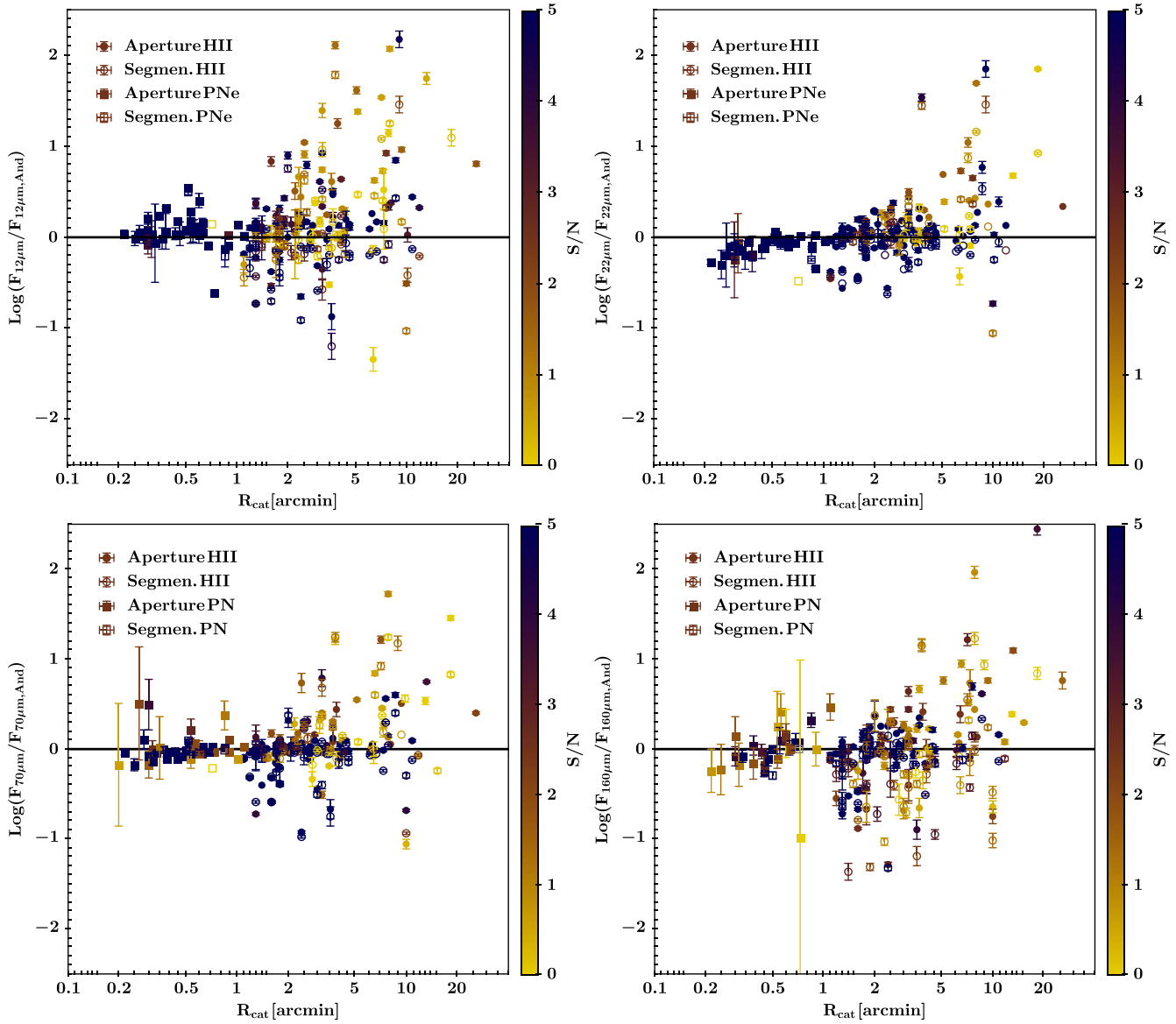

Figure 3. Distribution of flux differences between our methods and measurements of A12 as a function of the angular extension of the bubble. Fluxes from H II regions and PNe are displayed with circles and squares, respectively. For aperture photometry, filled dots are used, while dots for the segmentation photometry are empty. Radii are given in arcmin. The colour scale indicates the S/N characteristic of each of our measurements.

unconfused with nearby sources of emission. A12 provided the fluxes of these (126+43) bubbles at different IR bandpasses, including 12 and 22 μm from *WISE* and 70, 160, 250, 350 and 500 μm from *Herschel*.

We decided to apply our automated methods to the same object sample and to compare our estimated fluxes with those measured by A12, as a quality check of our results. They measured the fluxes emitted by the H II regions within an aperture of arbitrary size fixed manually and shaped in a way that includes all the associated emission at all wavelengths and excludes contaminating compact bright sources in the field. The assumption of a unique aperture is considered to be conservative and safe by the authors, as most of their H II regions are bright at IR wavelengths and have a similar morphology and angular extension at all wavelengths; however, this assumption implies some form of human intervention for deciding the shape. Considering the small angular size of PNe, their photometry is more sensitive to the choice of a unique aperture size for all the wavelengths, and thus they chose to adopt individual apertures at each bandpass. A12 published the measured fluxes along with the aperture radius used for each H II region and that at 24 μm for PNe.

Using radii from A12's catalogue as the dimension ($R_{\rm cat}$) of the bubbles and applying, as previously described, the two methods, we obtained the aperture and segmentation fluxes for each bubble. The comparison between our flux estimates and those from A12 are plotted in Fig. 2: aperture photometry for the H II regions (circles) and PNe (squares) is reported using filled dots, while the empty dots refer to the segmentation photometry. In Fig. 2, we report the comparison at 12, 22, 70 and 160 μm, as at these wavelengths the bubble is brighter and the estimate is less sensitive to the background variation, as discussed later in this section. A general agreement is visible among the flux measurements, especially for the PNe, while a larger scatter is present for the H II regions. The latter can be explained by a stronger contamination by the background to the

Downloaded from https://academic.oup.com/mnras/article-abstract/473/3/3671/4633601
by guest
on 13 March 2018

Table 1. Average difference between fluxes from this work and A12, where ΔLog has been calculated as in equation (2). The number of bubbles composing the '*detected*', '*bright*' and '*clipped*' samples (see Section 4.3) are given.

Aperture photometry					
Band	⟨ΔLog⟩	H II region		PN	
		Clip./bright/detect.	Bright/detect. (A12)	Clip./bright/detect.	Bright/detect. (A12)
12 μm[a]	0.11 ± 0.14	73/115/126	126/126	32/39/43	40/43
22 μm	0.01 ± 0.10	84/123/126	126/126	31/41/43	42/43
70 μm	−0.01 ± 0.06	75/122/126	126/126	33/43/43	43/43
160 μm	0.02 ± 0.14	81/120/126	126/126	24/28/43	31/43
250 μm	0.10 ± 0.20	81/121/124	126/126	17/19/43	21/43
350 μm	0.10 ± 0.22	84/120/126	126/126	14/14/43	16/43
500 μm	0.09 ± 0.23	83/120/126	126/126	11/11/43	12/43
Segmentation photometry					
Band	⟨ΔLog⟩	H II region		PN	
		Clip./bright/segmen.	Bright/detect. (A12)	Clip./bright/segmen.	Bright/detect. (A12)
12 μm[a]	−0.12 ± 0.11	57/94/94	126/126	4/4/4	40/43
22 μm	−0.02 ± 0.11	68/94/94	126/126	4/4/4	42/43
70 μm	−0.04 ± 0.07	59/97/97	126/126	4/4/4	43/43
160 μm	−0.18 ± 0.18	61/86/95	126/126	2/2/4	31/43
250 μm	−0.16 ± 0.26	52/62/98	126/126	1/1/4	21/43
350 μm	−0.18 ± 0.20	31/41/97	126/126	1/1/4	16/43
500 μm	−0.31 ± 0.15	21/30/98	126/126	1/1/4	12/43

Notes. [a]Similarly to A12, for *WISE* 12 μm, we have used a different DN-to-Jy conversion factor, equal to 2.9045×10^{-6} taken from the Explanatory Supplement of the preliminary data release products.

more extended bubbles. This is more evident in Fig. 3, in which flux ratios, expressed as

$$\Delta\mathrm{Log} = \mathrm{Log}F_{\lambda} - \mathrm{Log}F_{\lambda,\mathrm{And}} = \mathrm{Log}(F_{\lambda}/F_{\lambda,\mathrm{And}}), \quad (2)$$

are plotted as a function of bubble angular extension. We also note that among extended bubbles, those with a large difference in flux with respect to A12 have also a very low S/N.

At the same time, from a visual inspection of the few bubbles with a large scatter but high S/N (affecting in particular the H II regions), we found that the R_{cat} value reported by A12 could largely underestimate or overestimate the real dimensions of the bubble.

For this reason, in order to estimate an average ⟨Log $(F_{\lambda}/F_{\lambda,\mathrm{And}})$⟩, which could express the reliability of our methods, we removed values that differ more than 2σ from the mean. Average ⟨ΔLog⟩ are reported for each bandpass in Table 1. For the aperture photometry, we also provided the total number of bubbles from the A12 sample detected in our images, as well as the number of *bright* bubbles. We labelled bubbles with positive flux as *bright*, in contrast with those sources that are faint over a possibly complex background and have been consequently discarded. In a similar way, for segmentation photometry we reported the total number of detected bubbles successfully masked (*segmented*) and the corresponding number of bright bubbles. Finally, for both methods, we gave the sample of bright bubbles used to compute the average after the 2σ clipping (*clipped* bubbles). Similarly, for the A12 sample, we indicated the number of bright bubbles (i.e. bubbles with a no-null flux measurement by A12) over the total number. Results for bandpasses at $\lambda \geq 250$ μm are shown in Fig. 4.

In Fig. 5, we show the histograms of ΔLog for each bandpass: histograms are shown for both methods and refer to the distribution of the sample of bright bubbles and of the more limited sample, selected after the clipping (*clipped* sample). From Fig. 5, we can see that there is, in general, very good agreement between the two flux estimates. In particular, the difference between our aperture photometry and A12's is less than 5 per cent at 22, 70 and 160 μm, and increases to about ∼25 per cent at longer wavelengths, where we expect the emission from the bubble to be less intense relative to the background. The ⟨ΔLog⟩ at 12 μm is also ∼28 per cent, even though we used the old DN-to-Jy conversion factor (2.9045×10^{-6} from the Explanatory Supplement of the Preliminary data release products), as A12 did, to make the results consistent.

Moving to the comparison with the results obtained with the segmentation method, we found that the segmentation method has good agreement at shorter wavelengths (⟨$1 - F_{\lambda}/F_{\lambda,\mathrm{And}}$⟩ < 10 per cent), and a larger difference (∼25–35 per cent) at longer wavelengths. In particular, we can see that it tends to provide, on average, lower fluxes (⟨ΔLog⟩ < 0) – this is likely because the segmentation helps to better mask the flux falling in the aperture, allowing only that coming from the sources to be selected and removing the contaminating flux from the background. The origin of such differences could also be in the method, which could generally be too strong and is likely to remove the pixels of the more external parts of the bubble. However, as already discussed in Section 4.2, in this work we chose to obtain the masks from 70-μm images, knowing that 70-μm emission contours generally include those at shorter wavelengths. Moreover, we can assume that bubble shape at $\lambda >$ 70 μm does not change significantly, as emissions at such wavelengths originate from the same component of the bubble, namely the cold dust. As a consequence, the estimated discrepancies ⟨ΔLog⟩ can be more likely arisen from background contamination, which largely increases at redder bandpasses.

Downloaded from https://academic.oup.com/mnras/article-abstract/473/3/3671/4633601
by guest
on 13 March 2018

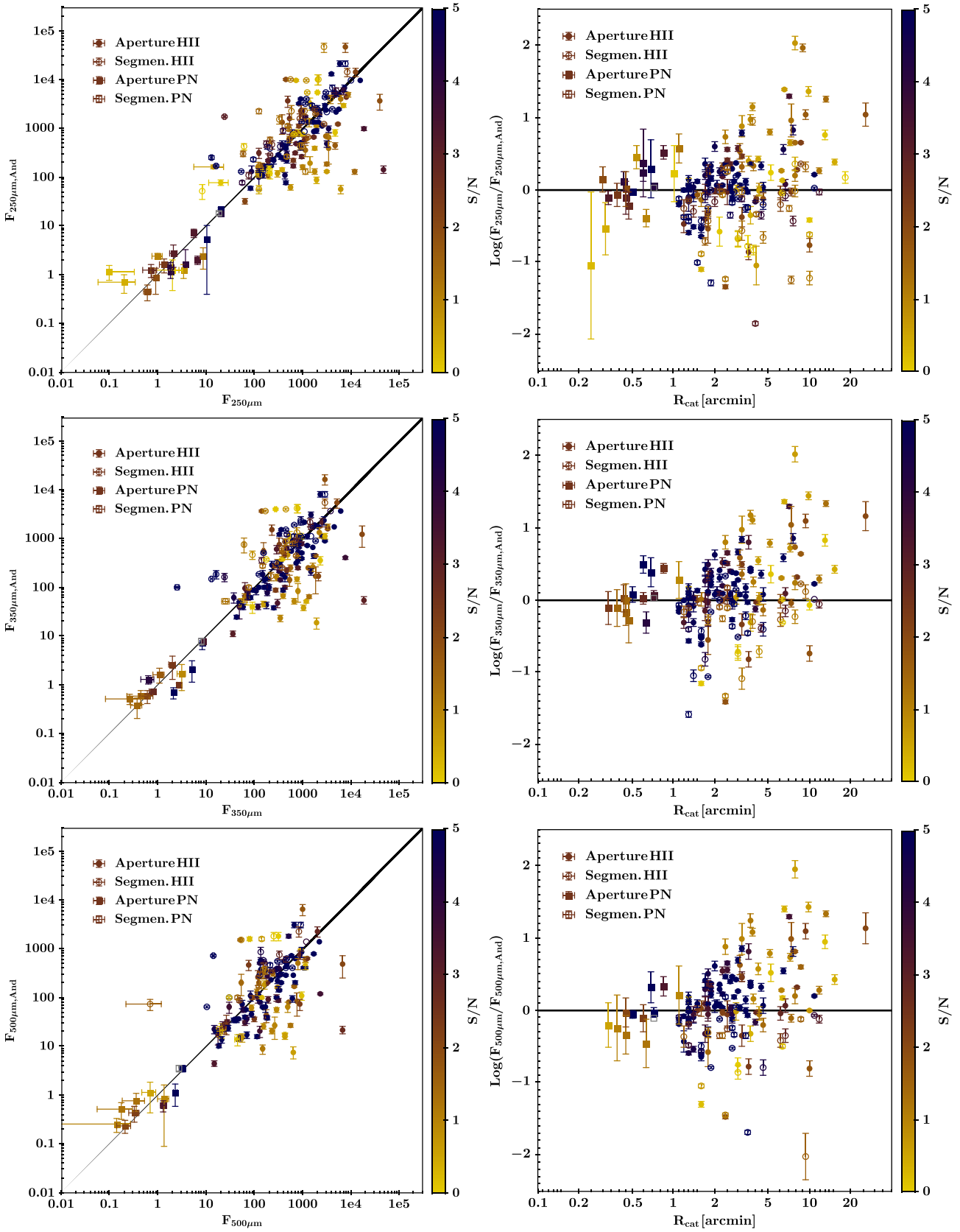

Figure 4. Left column: comparison of the photometry obtained with our automated methods and the results of A12 at 250, 350 and 500 μm. Fluxes from H II regions and PNe are reported with circles and squares, respectively. For aperture photometry, filled dots are used, while dots for the segmentation photometry are empty. Fluxes are given in Jy. Right column: distribution of flux differences between our methods and measurements of A12 as a function of the angular extension of the bubble. Radii are given in arcmin. In all plots, the colour scale indicates the S/N characteristic of each of our measurements.

Downloaded from https://academic.oup.com/mnras/article-abstract/473/3/3671/4633601
by guest
on 13 March 2018

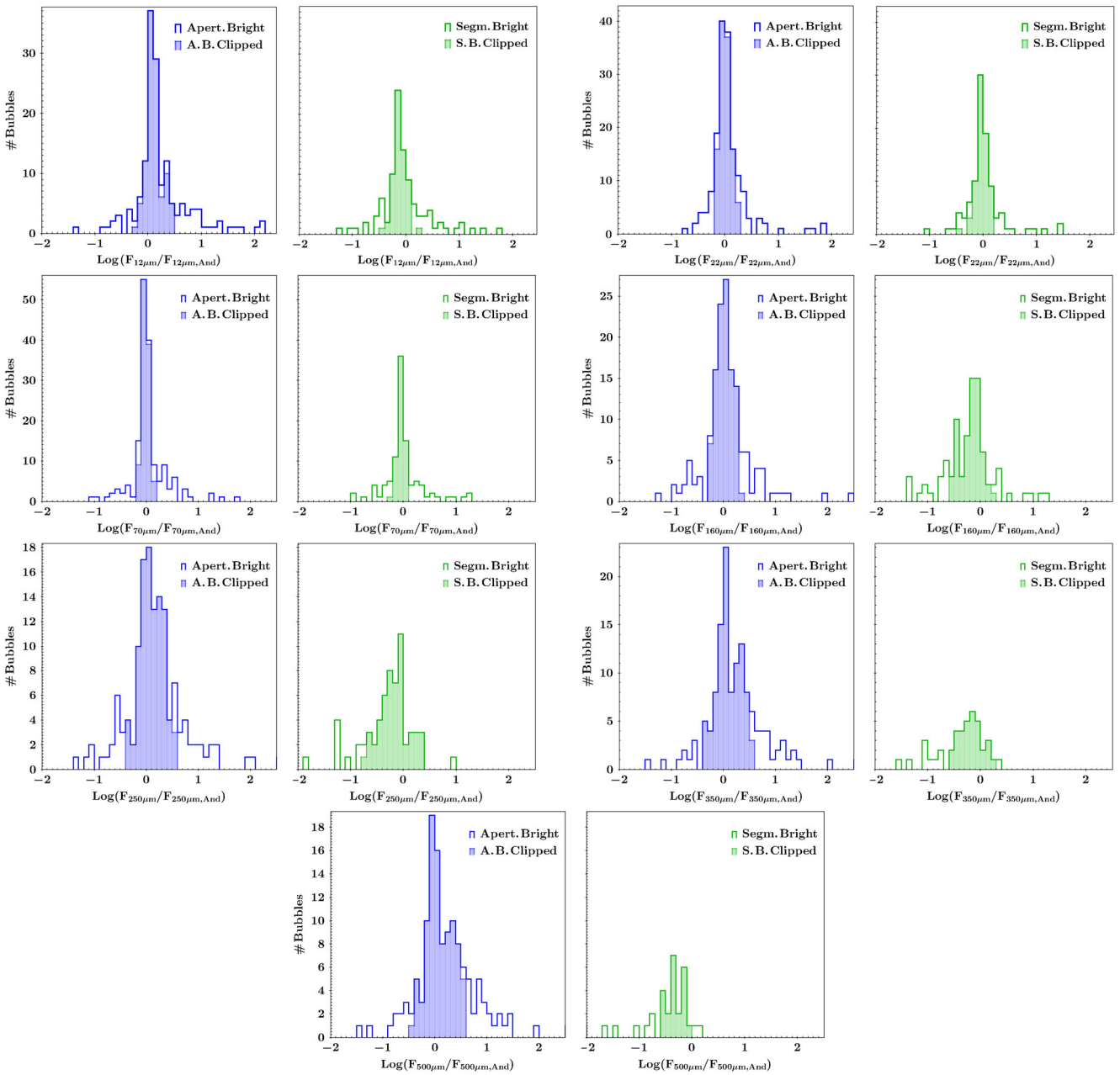

Figure 5. Histograms of the distribution of the difference ΔLog between fluxes from this work and A12. For each photometric method, bubble samples (H II regions plus PNe) are formed by the total sample of *bright* bubbles or by the limited sample ('*clipped*'), selected after the sigma-clipping (2σ level). These are reported with empty and filled histograms, respectively.

Finally, it is worth noticing that, when we considered the results on PNe of the segmentation method, we found that the active contours failed to find most of the bubbles, possibly because of their small angular size and/or because of a possible faint emission of such objects at 70 μm. We discuss in Section 6 the reason for this failure of the segmentation method to find bubble contours.

5 CATALOGUE FORMAT

As an example of the final catalogue, in Appendix B we show tables with the fluxes measured with the two methods for a collection of bubbles taken from the golden sample: *WISE* 12- and 22-μm values are given in Tables B1 and B2, respectively, and *Herschel* 70-, 160-, 250-, 350- and 500-μm values are given in Tables B3–B7.

All the tables give the source name followed by the Galactic longitude and latitude and the angular size ($R_{\rm cat}$) taken from Simpson et al. (2012) and used, as previously described (Section 2), in our work. Total flux (F_λ) and the associated uncertainty are given in Jy.

Missing flux estimates are indicated with '–' if the survey image only partially covers the bubble or if it has a high fraction of saturated/NaN pixels (>10 per cent), as in both cases the measurement would not be reliable. In the *WISE* images, there are 24 missing bubbles, all of them discarded because of a high fraction of saturated pixels, while for *Herschel* there are a maximum of 7 missing

Downloaded from https://academic.oup.com/mnras/article-abstract/473/3/3671/4633601
by guest
on 13 March 2018

Table 2. Bubble sample listed in the IR flux catalogue.

	Aperture photometry				Segmentation photometry			
Bandpass	Detected	Percentage[a]	Bright	Percentage[b]	Segmented	Percentage[c]	Bright	Percentage[d]
12 μm	1790	98.6%	1704	95.2%	1018	56.9%	1014	99.6%
22 μm	1791	98.7%	1726	96.4%	1019	56.9%	1017	99.8%
70 μm	1814	100.%	1763	97.2%	1024	56.5%	1024	100.%
160 μm	1814	100.%	1763	97.2%	1024	56.4%	663	64.7%
250 μm	1807	99.6%	1675	92.7%	1022	56.6%	351	34.3%
350 μm	1811	99.8%	1655	91.4%	1022	56.4%	208	20.3%
500 μm	1807	99.6%	1635	90.5%	1022	56.6%	143	14.0%

Notes. [a]Percentage of detected bubbles over the 1814 bubbles from the golden sample.
[b]Percentage of bright bubbles over the detected bubbles.
[c]Percentage of segmented bubbles over the detected bubbles.
[d]Percentage of bright bubbles over the segmented bubbles.

bubbles (for 250- and 500-μm images) with about half of them not completely covered. The number of remaining bubbles with 'positive' detection is reported in Table 2 (*detected* bubbles) for each bandpass together with their percentage with respect to the whole golden sample catalogue (1814 bubbles).

Flux estimates are indicated with '***' when the emission of the bubble is too faint (i.e. the source average flux per pixel is lower than the estimated average background level). Thus, in Table 2, we also report the total number of *bright* bubbles (all the bubbles with a flux estimate listed in the catalogue) and their percentage with respect to the number of detected bubbles. For the segmentation photometry, a measurement of the flux could also be missing (indicated with '-') when the active contour method fails to find the bubble (i.e. no segmentation mask corresponding to the bubble is produced). Also, in this case we report the number of *segmented* bubbles with the relative fraction over the detected sample, and the number of *bright* bubbles along with the fraction with respect to the segmented sample. Thus, Table 2 gives a global view of what is available in the entire flux catalogue.

6 DISCUSSION

Fluxes obtained from the aperture and segmentation method are presented in Fig. 6. For each bubble, we plotted the aperture photometry flux against the segmentation photometry flux, with the size of the dots proportional to the logarithm of the bubble radius ($R_{\rm cat}$) and the colour scaled based on the S/N of the corresponding aperture flux estimation. The latter efficiently conveys the brightness of a source over the possible complex background. We define the ratio between the two flux measurements for each bubble as

$$\Delta M_\lambda = \mathrm{Log}F_{\lambda,\mathrm{Ap.}} - \mathrm{Log}F_{\lambda,\mathrm{Segm.}} = \mathrm{Log}(F_{\lambda,\mathrm{Ap.}}/F_{\lambda,\mathrm{Segm.}}), \quad (3)$$

and plot it as a function of the angular dimension of the bubble in Fig. 7. In Table 3, we report the average $\langle\Delta M_\lambda\rangle$ value for each bandpass, obtained after clipping values more than 3σ away from the average. The total numbers of detected/clipped bubbles in the sample are also given.

A very good agreement between aperture and segmentation photometry is visible at 70 μm, where $\langle F_{\lambda,\mathrm{Ap.}}/F_{\lambda,\mathrm{Segm.}}\rangle$ is close to 1, giving a relative difference of around 7 per cent. This bandpass better quantifies the deviation between the two methods, as the segmentation masks are produced using the images taken at this wavelength, and thus the contours best trace the bubble shape. Consequently, we can assess that, at 70 μm, the aperture photometry fluxes are generally slightly larger than the segmentation photometry fluxes. We also found this when comparing the two methods at the other bandpasses, convolving the mask to reproduce instrumental differences from 70-μm images and also assuming a physically similar shape. Higher aperture flux can likely be ascribed to the contamination in the aperture method from the local background flux that cannot be totally removed by subtracting the average level and/or that falls within the aperture but outside the bubble contours as defined by the segmentation method. The effects of a complex background could explain why ΔM_λ increases at larger radii ($R_{\rm cat} > 2$ arcmin), as visible in Fig. 7. This could also explain why bubbles for which ΔM_λ is below zero ($F_{\lambda,\mathrm{Ap.}} < F_{\lambda,\mathrm{Segm.}}$) all have a low S/N. Thus, the fact that low S/N bubbles preferentially lead to $\Delta M_\lambda < 0$ seems to suggest that segmentation is the better choice, when available, for the flux measurements of extended sources.

Table 3. Average difference between bubble fluxes measured with aperture and segmentation photometric methods. The number of 'clipped' bubbles over the total number of bubbles is given, and these turn out to be 'bright' after the application of both methods.

Band	$\langle\Delta M_\lambda\rangle$	Clipped/bright bubbles
12 μm	0.06 ± 0.11	954/1008
22 μm	0.06 ± 0.07	950/1012
70 μm	0.03 ± 0.05	935/1020
160 μm	0.23 ± 0.37	632/663
250 μm	0.28 ± 0.47	336/346
350 μm	0.25 ± 0.52	203/206
500 μm	0.18 ± 0.47	136/138

The good agreement between aperture and segmentation photometry stands out, especially at short wavelengths, with a difference $|\Delta M_\lambda| < 0.1$ for 65, 68 and 81 per cent of the cases at 12, 22 and 70 μm, respectively. The distribution becomes more widely spread at 160 μm, as visible in Figs 6 and 7, and as indicated by $\langle\Delta M_\lambda\rangle$ in Table 3. This is a consequence of a dominant emission from the background that, moving redward, increasingly contaminates the flux measurements. At 160 μm, the number of bubbles with $|\Delta M_\lambda| < 0.1$ drops significantly to 19 per cent and, at 250 μm, to 14 per cent, with an average relative difference that could reach ∼50–90 per cent.

As shown in Table 2, we found that the active contour segmentation method failed for about 45 per cent of the detected bubbles. The reason for such a fraction of failed segmentation could be the presence of a possibly complex background, which is expressed by a low S/N of the measurements.

Downloaded from https://academic.oup.com/mnras/article-abstract/473/3/3671/4633601
by guest
on 13 March 2018

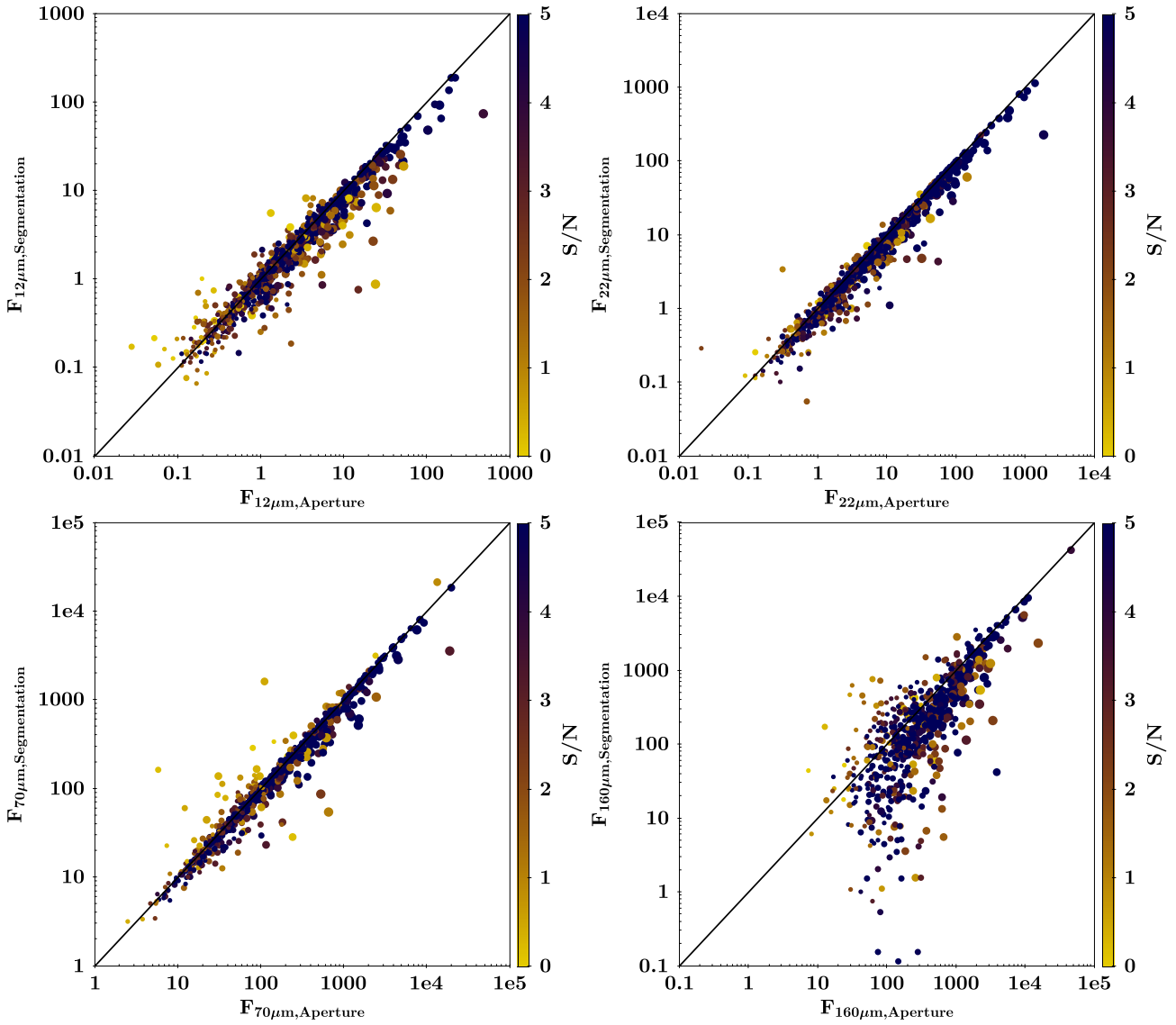

Figure 6. Comparison of flux estimates using the aperture photometry against the segmentation photometry. Dot size is proportional to the logarithm of the bubble radius ($R_{\rm cat}$) and the colour scales are based on the S/N of the relative aperture flux estimation.

We split the bubbles into *extended* ($R_{\rm cat} > 60$ arcsec) and *compact* ($R_{\rm cat} \leq 60$ arcsec) sources, and we show in Fig. 9 the relative distribution of bubbles with failed segmentation as a function of the S/N. Because no S/N is estimated for non-segmented bubbles, for consistency we use that from aperture photometry instead. As expected, extended bubbles with strong contamination or the presence of a structurally complex background affect the boundary found by the algorithm. Indeed, at 70 μm, the fraction of extended bubbles with failed segmentation is equal to 55 per cent, and 92 per cent of these have a S/N lower than 5 (see Fig. 9). This fraction is ∼70 per cent if we include segmented bubbles.

For compact bubbles, this effect seems to affect the distribution less, as they are characterized by a lower fraction of unsegmented bubbles with low S/N than extended bubbles: 40 per cent of compact bubbles have failed segmentation, and 76 per cent of these are characterized by a S/N < 5, corresponding to a slightly smaller fraction (∼64 per cent) compared to the whole low S/N sample. This confirms that extended bubbles are more affected by the failures of the segmentation method because of the background contamination.

Average $\langle \Delta M_\lambda \rangle$ is always positive at all bandpasses and increases when moving to longer wavelengths: the relative difference between the two methods obtained from ΔM_λ is less than 15 per cent for 12 and 22 μm and goes up to 50–70 per cent at longer wavelengths with a peak at 250 μm (∼93 per cent). This effect clearly points to a relevant flux contamination from the background. This is supported also by the steep drop in the number of bright bubbles (see Table 3). In Fig. 10, we show the cumulative distributions of segmented compact and extended bubbles at 70 and 250 μm as a function of the S/N of the flux measurements. The S/N characterizing the bubbles decreases at longer wavelengths due to a stronger background emission and/or to a weaker source emission: the fraction of extended bubbles with S/N >5 goes from 53 per cent at 70 μm down to 21 per cent at 250 μm, while for compact bubbles the fraction changes from 72 to 39 per cent at 70 and 250 μm, respectively.

Downloaded from https://academic.oup.com/mnras/article-abstract/473/3/3671/4633601
by guest
on 13 March 2018

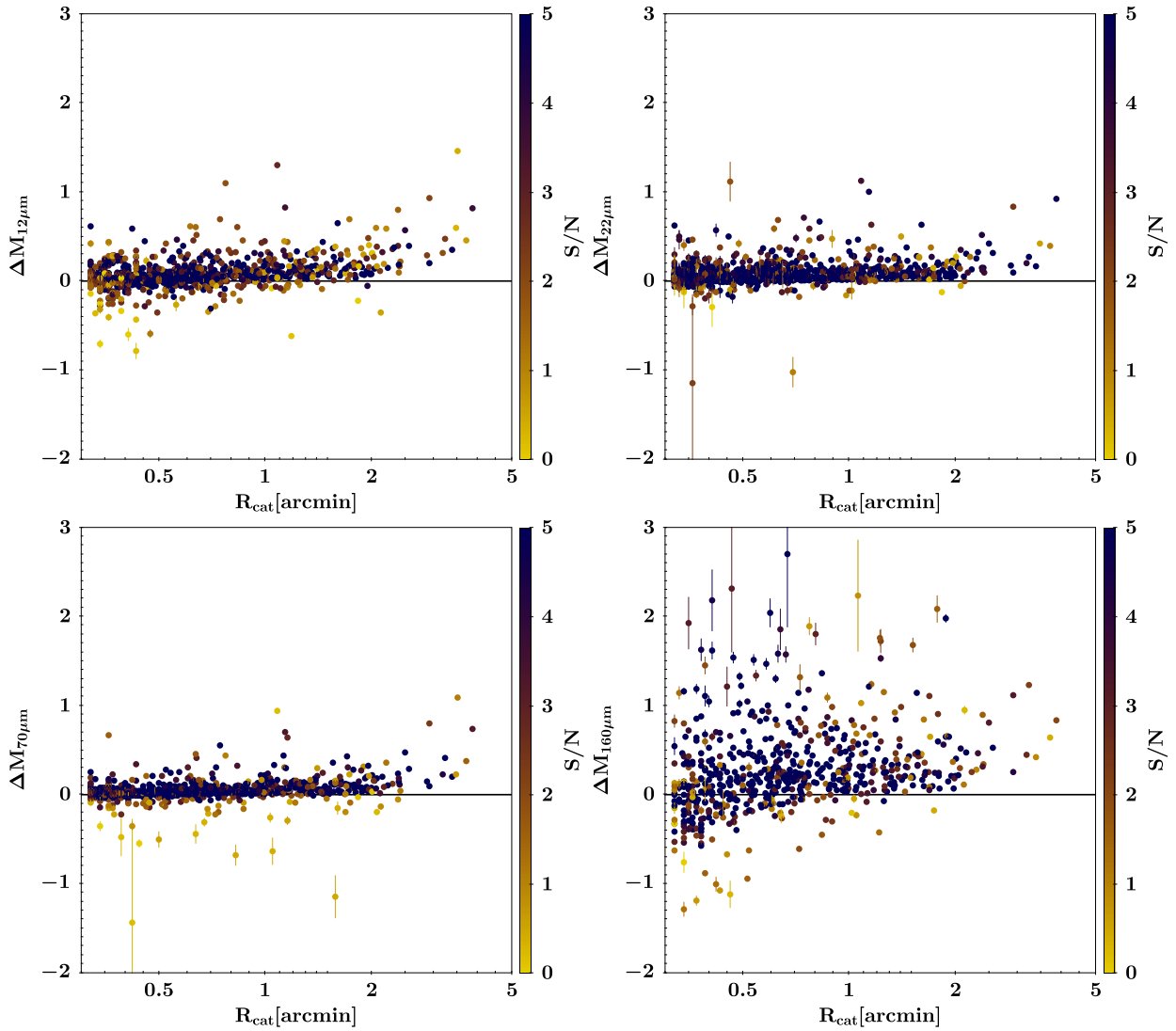

Figure 7. Distribution of flux differences between aperture and segmentation photometric methods as a function of the angular extension of the bubble. Radii are given in arcmin. The colour scales are based on the S/N of the relative aperture flux estimation.

Thus, given the underestimation of the total emitted flux of the segmentation method with respect to the aperture observed in Fig. 6 and obtained from the analysis of low S/N bubbles, the segmentation method demonstrates that it is closer to the real flux than the aperture method. Nevertheless, when using this method, it should be taken into consideration that the real shape of the bubble contours at $\lambda \neq 70$ μm could differ from that assumed by using the segmentation masks.

7 CONCLUSIONS

This work, which emerged from the wide framework of the VIALACTEA project,[5] has been inspired by the unique opportunity, offered by the *Herschel* telescope because of its sensitivity and its large wavelength coverage in the far-IR, to derive the physical conditions in Galactic bubbles, whose origins can radically differ being the yield of different stages of star evolution. We have taken advantage of the availability of the wide image dataset collected from the Hi-GAL survey, flanking it with the *WISE* survey data that sample emissions at shorter wavelengths, and we have produced the most extensive catalogue of IR fluxes of extended sources. Thus, in this work, we present the fluxes of a golden sample of 1814 Galactic bubbles taken from Simpson et al. (2012), acquired at 12-, 22-, 70-, 160-, 250-, 350- and 500-μm bandpasses.

We used two approaches for the flux estimation: a classical aperture photometry and a more innovative method, based on the use of segmentation masks, produced by an image analysis algorithm, called active contours, which defines the boundaries of the bubbles (see Appendix A for a brief explanation of the method). In both methods, we used the bubbles' dimensions provided by Simpson et al. (2012) to define a circular aperture region centred on the bubble centroid where we estimated the source fluxes and an annular region around it for the local average background level definition.

Fluxes obtained with both aperture and segmentation photometry were checked by comparing them with those of a more limited sample of H II regions and PNe from A12, obtained with an interactive method. We found very good agreement, especially with

[5] http://vialactea.iaps.inaf.it

Downloaded from https://academic.oup.com/mnras/article-abstract/473/3/3671/4633601
by guest
on 13 March 2018

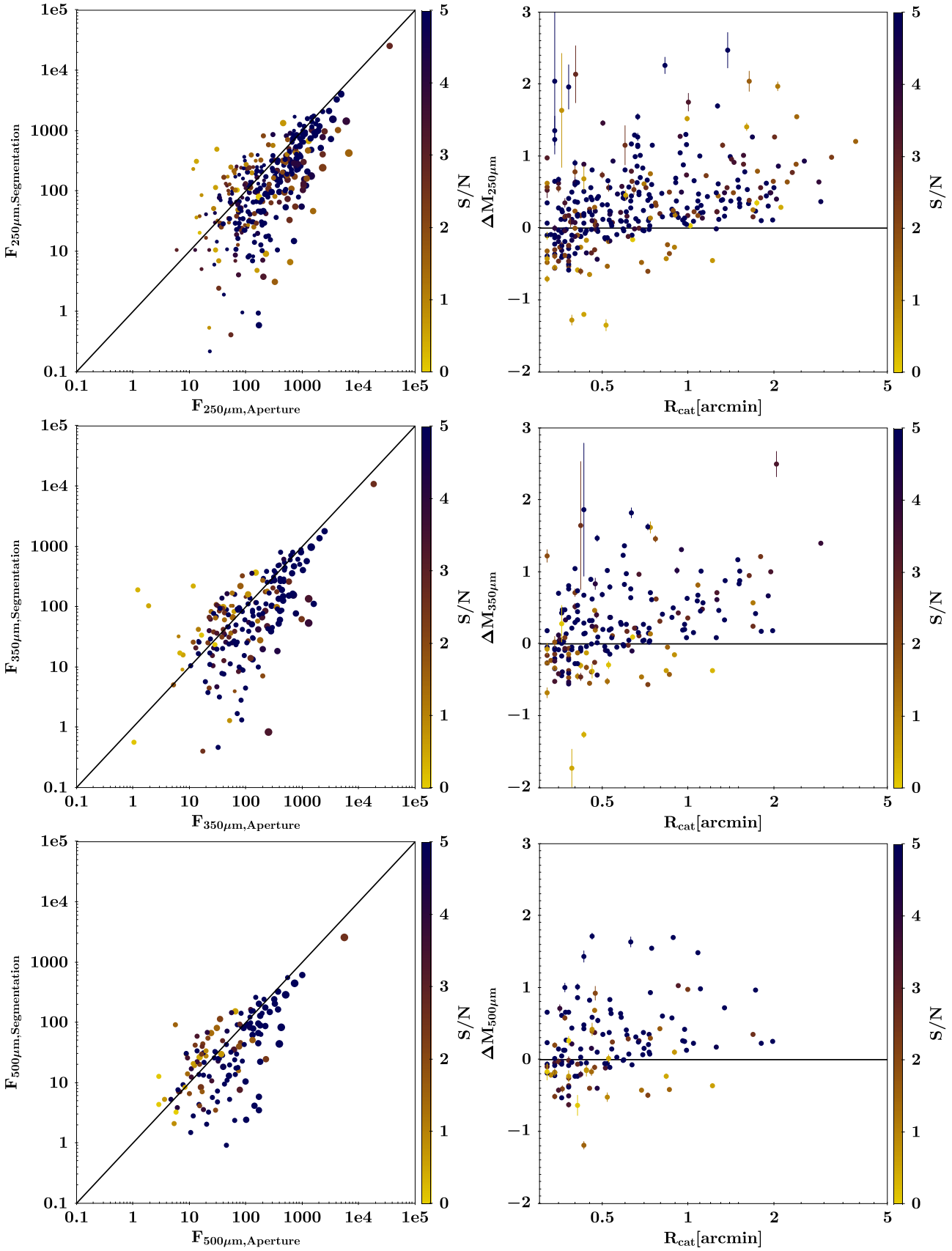

Figure 8. Left column: comparison of flux estimates using the aperture photometry against the segmentation photometry. Dot size is proportional to the logarithm of the bubble radius (R_{cat}). Right column: distribution of flux differences between aperture and segmentation photometric methods as a function of the angular extension of the bubble. Radii are given in arcmin. For all the plots, colour scales are based on the S/N of the relative aperture flux estimation.

Downloaded from https://academic.oup.com/mnras/article-abstract/473/3/3671/4633601
by guest
on 13 March 2018

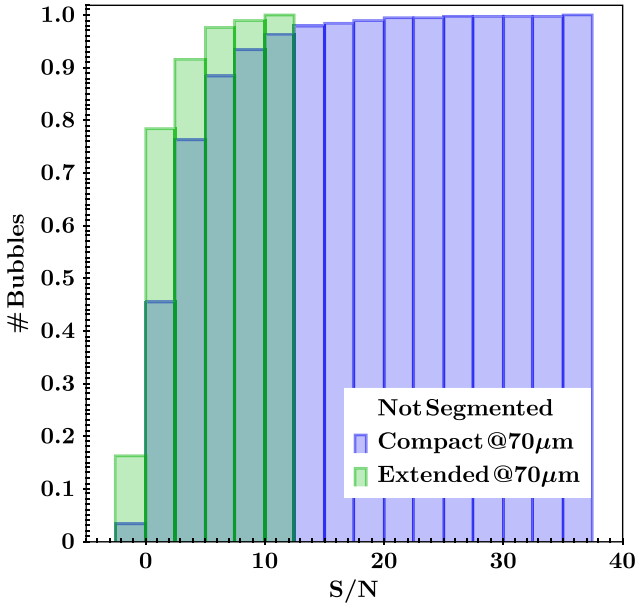

Figure 9. Cumulative distribution of bubbles with failed segmentation at 70 μm as a function of the S/N from aperture flux estimation.

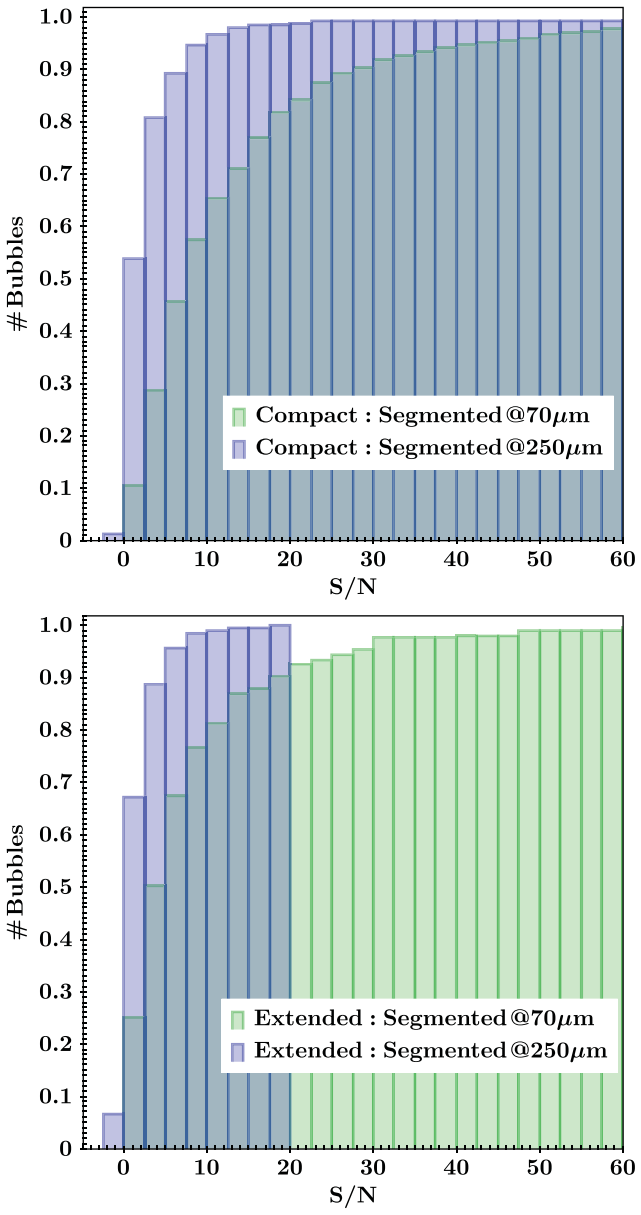

Figure 10. Cumulative distribution of segmented bubbles at 70 and 250 μm as a function of the S/N of the aperture flux estimation.

the aperture method results. However, segmentation photometry seems to work better at short wavelengths but fails for compact objects, for which the segmentation algorithm shows a high failure rate in producing bubble masks.

Finally, we compared fluxes of bubbles in the golden sample obtained with the two methods, finding very good agreement especially at the shorter wavelengths (the average difference does not exceed 15 per cent). Generally, aperture photometry fluxes turn out to be larger than the segmentation photometry fluxes, possibly a consequence of a contaminating complex background, whose subtraction can be a tricky task. Indeed, this effect becomes stronger at long wavelengths (>160 μm) where background dust emission increases.

With this work, we offer for the first time a wide catalogue of bubble IR fluxes, produced using fully automated methods. This kind of approach, together with automated algorithms using for instance data mining capabilities for the source extraction of extended sources or the automated definition of the source contours (e.g. Carey et al., in preparation; Riggi et al. 2016), is a necessary choice in the astrophysical data analysis considering the new generation instruments (e.g. LSST in the optical, *JWST* in the IR and SKA at radio frequencies), which will survey wide sky regions, providing a gigantic amount of data.

Querying the SIMBAD astronomical database (Wenger et al. 2000),[6] we checked whether the bubbles in the golden sample have been identified with a specific star evolution event. We considered all the objects in a circular area of radius $R_{\rm cat}$ centred on each bubble centroid coordinates and we selected the one at the minimum distance as the literature object associated with the bubble (assuming to be negligible the probability of false matches coming from perspective coincidences). Finally, we split the objects into H II regions, evolved stars (which includes LBV stars, AGB and post-AGB stars, SNRs, PNe, etc.) and unknown. We noticed that the fraction of bubbles that are classified as H II regions is highest (60 per cent), against the very low 2 per cent of evolved stars (see Fig. 11). Fractions do not change significantly if we split bubbles into *extended* and *compact*, as done in the previous section. In any case, a large fraction (38 per cent) remain unclassified. This finding, together with the future perspective of the large amount of available data, strengthens the need for an automated method for bubble classification, possibly based on their SED and/or on their morphology at different wavelengths. This issue extends beyond the purpose of this work, but it will be a matter of discussion in a forthcoming paper.

[6] We noticed that H II regions identified by Anderson et al. (2014), as well as Anderson et al. (2011) and Paladini et al. (2003), were not included in the SIMBAD database. Thus, we additionally check these catalogues for our statistics.

Downloaded from https://academic.oup.com/mnras/article-abstract/473/3/3671/4633601
by guest
on 13 March 2018

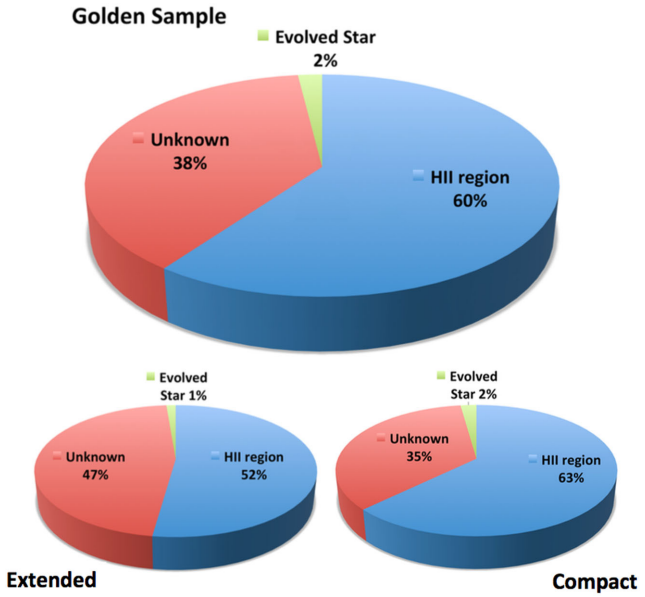

Figure 11. Fraction of classified/unclassified bubbles in the golden sample from the SIMBAD database.

ACKNOWLEDGEMENTS

The authors acknowledge the anonymous referee for very useful comments that helped to improve the paper. This work is part of the VIALACTEA Project, a Collaborative Project under Framework Programme 7 of the European Union, funded under Contract 607380, which is hereby acknowledged. FB acknowledges support from the VIALACTEA Project. *Herschel* is an ESA space observatory with science instruments provided by European-led Principal Investigator consortia and with important participation from NASA. PACS has been developed by a consortium of institutes led by MPE (Germany) and including UVIE (Austria); KUL, CSL, IMEC (Belgium); CEA, OAMP (France); MPIA (Germany); IAPS, OAP/OAT, OAA/CAISMI, LENS, SISSA (Italy); IAC (Spain). This development has been supported by the funding agencies BMVIT (Austria), ESA-PRODEX (Belgium), CEA/CNES (France), DLR (Germany), ASI (Italy) and CICYT/MCYT (Spain). SPIRE has been developed by a consortium of institutes led by Cardiff University (UK) and including University of Lethbridge (Canada); NAOC (China); CEA, LAM (France); IAPS, University of Padua (Italy); IAC (Spain); Stockholm Observatory (Sweden); Imperial College London, RAL, UCL-MSSL, UKATC, University of Sussex (UK); Caltech, JPL, NHSC, University of Colorado (USA). This development has been supported by national funding agencies: CSA (Canada); NAOC (China); CEA, CNES, CNRS (France); ASI (Italy); MCINN (Spain); Stockholm Observatory (Sweden); STFC (UK); and NASA (USA).

This publication makes use of data products from the *WISE*, which is a joint project of the University of California, Los Angeles, and the Jet Propulsion Laboratory/California Institute of Technology, funded by the National Aeronautics and Space Administration. This research has made use of the SIMBAD database, operated at CDS, Strasbourg, France. This research made use of MONTAGE. It is funded by the National Science Foundation under Grant Number ACI-1440620, and was previously funded by NASA's Earth Science Technology Office, Computation Technologies Project, under Cooperative Agreement Number NCC5-626 between NASA and the California Institute of Technology.

REFERENCES

Akram F., Kim J. H., Lim H. U., Choi K. N., 2014, Computational and Mathematical Methods in Medicine, 194614
Anderson L. D., Bania T. M., Balser D. S., Rood R. T., 2011, ApJS, 194, 32
Anderson L. D., Zavagno A., Barlow M. J., García-Lario P., Noriega-Crespo A., 2012, A&A, 537, 1 (A12)
Anderson L. D., Bania T. M., Balser D. S., Cunningham V., Wenger T. V., Johnstone B. M., Armentrout W. P., 2014, ApJS, 212, 1
Balog Z. et al., 2014, ExA, 37, 129
Bendo G. J. et al., 2013, MNRAS, 433, 3062
Benjamin R. A. et al., 2003, PASP, 115, 953
Carey S. J. et al., 2009, PASP, 121, 76
Churchwell E. et al., 2006, ApJ, 649, 759
Churchwell E. et al., 2007, ApJ, 670, 428
Deharveng L. et al., 2010, A&A, 523, A6
Griffin M. J. et al., 2010, A&A, 518, L3
Hummel R. A., 1977, Computer Graphics and Image Processing, 6, 184195
Lankton S., Tannembaum A., 2009, IEEE Trans. Image Process., 17, 2029
Mizuno D. R. et al., 2010, AJ, 139, 1542
Molinari S. et al., 2010, A&A, 518, L100
Molinari S. et al., 2016, A&A, 591, A149
Paladini R., Burigana C., Davies R. D., Maino D., Bersanelli M., Cappellini B., Platania P., Smoot G., 2003, A&A, 397, 213
Paladini R. et al., 2012, ApJ, 760, 149
Pilbratt G. L. et al., 2010, A&A, 518, L1
Poglitsch A. et al., 2010, A&A, 518, L2
Riggi S. et al., 2016, MNRAS, 460, 1486
Rogers E., Zack G. W., 1977, J. Histochem. Cytochem., 25, 11
Simpson R. J. et al., 2012, MNRAS, 424, 2442
Tielens A. G. G. M., 2008, ARA&A, 46, 289
Traficante A. et al., 2011, MNRAS, 416, 2932
Volk K., Kwok S., 2003, in Kwok S., Dopita M., Sutherland R., eds, Proc. IAU Symp. Vol. 209, Planetary Nebulae: Their Evolution and Role in the Universe. Astron. Soc. Pac. San Francisco, p. 303
Wachter S., Mauerhan J. C., Van Dyk S. D., Hoard D. W., Kafka S., Morris P. W., 2010, AJ, 139, 2330
Wang L., He L., Mishra A., Li C., 2009, Signal Processing, 89, 2435
Wenger M. et al., 2000, A&AS, 143, 9
Wright E. L. et al., 2010, AJ, 140, 1868
Xie X., Mirmehdi M., 2008, IEEE Trans. Pattern Anal. Mach. Intell., 30, 632
Yang Q., Boukerroui D., 2012, in Proc. IEEE Int. Symp. Biomedical Imaging. IEEE, New York, p. 1096
Yilmaz A., Javed O., Shah M., 2006, ACM Computing Surveys, 38, 13

APPENDIX A: THE ACTIVE CONTOURS METHOD FOR SEGMENTATION

Active contours are a family of popular curve deformation techniques that are often applied within computer vision for the unsupervised segmentation of image objects. Their simple mode of operation has allowed them to be applied to a variety of different problems (Akram et al. 2014; Lankton & Tannembaum 2009; Yilmaz, Javed & Shah 2006). They are especially useful in instances where the use of supervised machine-learning approaches is implausible. This is because labelled data are expensive to generate and the robustness of these techniques makes them good candidates for situations where there is a lack of expert annotations. However, the drawback of most contouring methods is that they come with the caveat that parameters have to be substantially adjusted before segmentations will meet human expectations. For example, a well-established, and parameter heavy, active contour model is the localized variant (Lankton & Tannembaum 2009; Wang et al. 2009; Yang & Boukerroui 2012) which evaluates contour deformation functions within the bounds of predefined kernels. The size of the

Downloaded from https://academic.oup.com/mnras/article-abstract/473/3/3671/4633601
by guest
on 13 March 2018

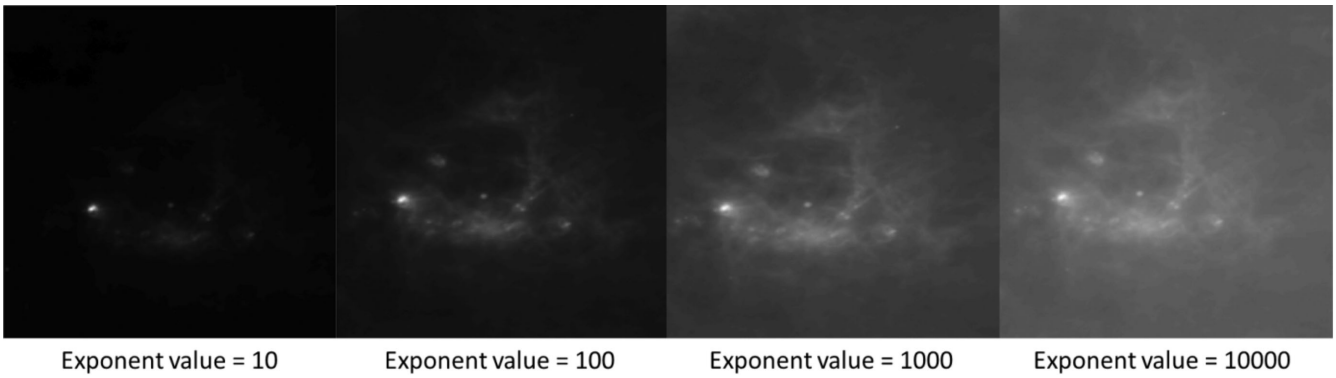

Figure A1. The result of using a range of different exponent values. The gradient magnitudes of these are correlated against those of the Log of the magnitude of the original data so that appropriate exponent values can be found.

kernels largely dictates the end segmentation result and as they have to be defined a priori, its use in real-world problems is often limited. Therefore, this paper addresses the above issue with a novel generic adaptive kernel selection scheme that also makes use of the sign of magnetostatic forces (Xie & Mirmehdi 2008). The use of signed electrostatic information enables textured foreground regions to be delineated from low gradient background areas. However, as astronomical images are composed of complex objects of varying intensity, the segmentation results of magnetostatic active contours cannot be relied upon, and more appropriate results are achieved when this technique is aided by local statistical information. The main steps adopted in this paper are reported in the following text, while a more detailed description of the method is given in Carey et al. (in preparation).

A1 Preprocessing

The above approaches work best when the image data under consideration are made more amenable to segmentation. In this work, preprocessing amounted to: adjusting the dynamic range of the original image data by selecting a Log transformation coefficient, which maximized the correlation between the transformed and the Log of the original data's numerical gradients; locally maximizing the contrast (defined as the difference in intensity between local pixels) of the transformed data; data smoothing and compression via a discrete wavelet transformation and appropriately initializing the active contour algorithm.

A1.1 Automatic Log exponent selection

Log transformation is a standard tool used in astronomy and it results in the compression of the dynamic range of the data. The skewness of the original image, where there are only a few pixels with high intensity values, means that if active contours were applied to these data, then they will only fit around very bright objects. Therefore, the difference in intensity between high- and low-valued pixels needs to be decreased, and this is accomplished by Log transformations. When too high exponent values are used in this process, more pixels will reach the maximum transformed intensity value of 255. This will make the boundaries of the bubble features more difficult to locate, as is evident from Fig. A1 where the definition of the edges of the image object has varying degrees of ambiguity over the range of exponent values used. Notice that when using a value of 10 000, the bright source in the bottom left of the image dominates the local region and the true edge of the object is lost. Therefore, similar problems as when using the original image data will persist. The same is true when using exponent values that are too low, where differences in pixel intensity values with respect to the images background are lost. The edges of the transformed data will be weak when definition is lost and so correlating the transformed images gradient with that of the Log of the gradient magnitude of the original will mean that an exponent value is selected that preserves as much authentic boundary information as possible.

A1.2 Local adaptive contrast histogram equalization

The selection of an appropriate Log transformation preserves as much boundary information as possible but the definition of the objects boundaries and their contrast with respect to the background can still be poor (due to the inherent skewness of the original data). Therefore, a tiling process, known as locally adaptive contrast histogram equalization (LACHE), was used to adjust the local pixel intensity histograms of patches of the original image (Hummel 1977). In this paper, a local tile of 40×40 pixels was used. The adjustments result in the stretching of the local histograms so that very weak pixels become more apparent. This greatly improves the definition of the bubble features, as is apparent when Fig. A2 is compared to those present in Fig. A1.

A1.3 Discrete wavelet transformation

The localized enhancement of the image features helps in the segmentation process but the large variations introduced by the above process need to be corrected for. In this instance, this was facilitated by a discrete wavelet transformation (DWT). As LACHE is a local technique, errors in enhancement can occur at the edges of the local tiles that this algorithm uses. This can affect where the boundaries of bubble object reside and so this essential smoothing process enables the active contours to better fit the features of interest. DWT not only smooths out the data but also reduces the size.

A1.4 Initialization

The starting position of the active contour, from which it will grow, also has a large impact on the end segmentation result. In this paper's approach, the incorporation of magnetostatic forces relieved this difficulty to an extent, but the contours still needed to be started fairly close to object of interest. For example, every pixel in an image will

Downloaded from https://academic.oup.com/mnras/article-abstract/473/3/3671/4633601
by guest
on 13 March 2018

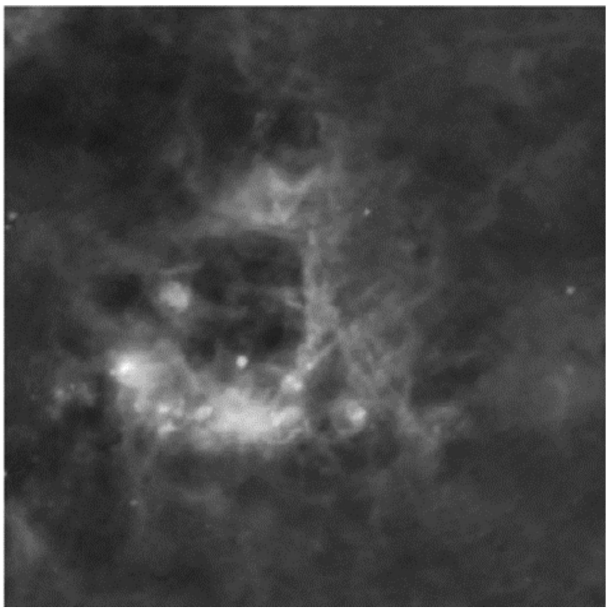

Figure A2. The result of using the 1000 exponent transformed image of Fig. A1 with localized contrast enhancement with a tile size of 40 × 40 pixels.

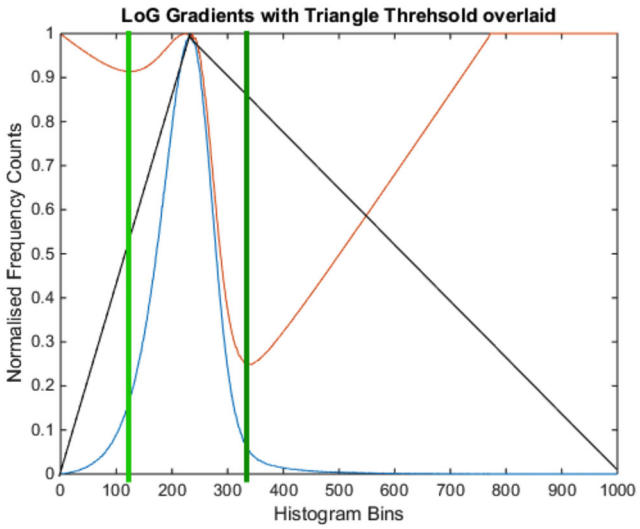

Figure A3. A histogram of the original image's Log gradients. The blue line is the histogram, the black lines are the triangles formed by the triangle thresholding, the red lines are the distances of the histogram's bin counts away from their nearest triangle hypotenuse and the green lines are the selected threshold points. Please note that the red lines contained in the chart do not relate to the *y*-axis. Depending on the distance calculation used, the calculated distance can be either negative or positive. In this case, the negative output was used so the largest negative value was found for the selected thresholds.

have gradient and these will not necessarily correspond to image objects of interest. Therefore, the simple use of thresholding to provide active contour initialization points will mean that contours could grow around undesired structures within the data. To avoid this, the triangle thresholding algorithm (Rogers & Zack 1977) was used with the Log of the gradient magnitude of the original image data. Its mode of operation is demonstrated in Fig. A3. In this

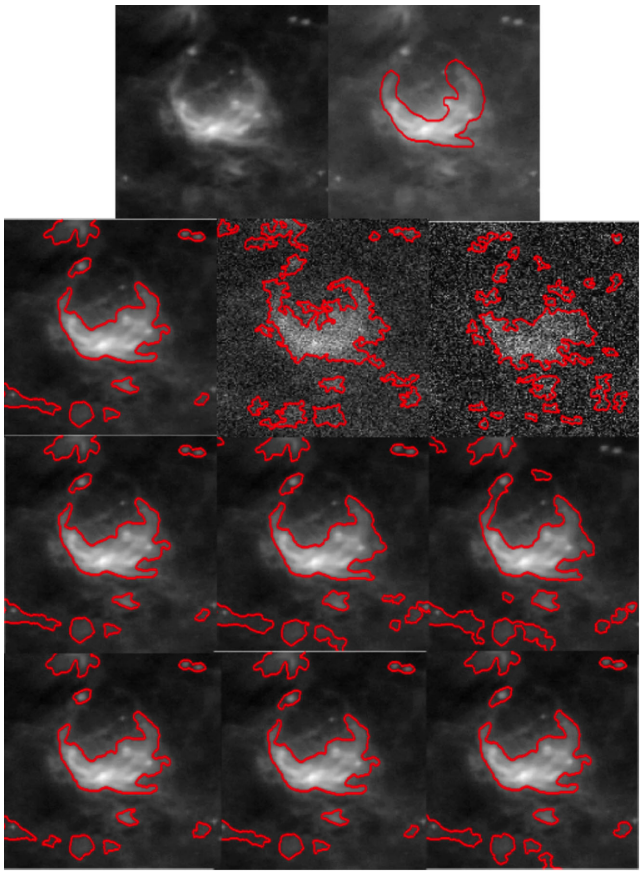

Figure A4. Effect of noise and parameters on segmentation quality. Top row: the original data and an astronomer ground truth in red. Second row: the effect of Gaussian noise of zero mean and 0, 0.01 and 0.03 variance on the segmentation. Third row: the effect of different τ values (0.5, 1 and 2) with a fixed initial kernel size. Fourth row: the effect of different initial kernel sizes (10 × 10 pixels, 20 × 20 pixels and 40 × 40 pixels).

technique, a histogram is formed from the Log gradient magnitude image. Its maximum peak, the first and last non-empty histogram bins, are found so that two triangles can be formed between its two extrema, and the largest concavity (the largest distance) found for each triangle allows an objective threshold to be found for automatic active contour initialization. Because two thresholds are found, the highest is selected for this segmentation pipeline, assuming that celestial objects are usually brighter than their background, as is usually observed.

A2 Adaptive kernel selection

Once the data are made more amenable to segmentation, active contours can be used for segmentation. The approach taken in this paper relied upon the use of gradient and local statistical information. Gradient information was incorporated via magnetostatic forces and local statistical information was acquired by the use of an adaptive kernel selection scheme. In traditional approaches, the size of the local area used in the collection of image statistics is predetermined, but this is unlikely to reflect the changing content of an image over which the contour evolves. To reflect this changing texture, an initial kernel size, set to be 20 × 20 pixels in this paper, is used to compute the local parametric Bhattacharyya distance between the inside and outside regions of an evolving contour,

Downloaded from https://academic.oup.com/mnras/article-abstract/473/3/3671/4633601
by guest
on 13 March 2018

which is defined as

$$BD = \exp\left\{-\frac{1}{4}\ln\left[\frac{1}{4}\left(\frac{\sigma_{\rm in}^2}{\sigma_{\rm out}^2}+\frac{\sigma_{\rm out}^2}{\sigma_{\rm in}^2}+2\right)\right] + \frac{1}{4}\left[\frac{(\mu_{\rm in}-\mu_{\rm out})^2}{\sigma_{\rm in}^2+\sigma_{\rm out}^2}\right]\right\}. \quad \text{(A1)}$$

Here, μ and σ are the respective mean and standard deviations of the intensities on the inside and outside of a local region around the evolving contour. This gives a normalized measure of how similar the inside and outside regions of the evolving curve are, allowing large kernels to be selected for regions of homogeneity and small sizes for areas of texture. The weighting of this with a user-defined parameter, τ (set to be 0.5 throughout), allowed kernel sizes to be selected in a single pass approach by multiplying equation (A1) with a maximum desired kernel size. Once appropriate kernel sizes have been selected, any localized regional evolution function can be used. In this instance, the following function was used to guide contours towards salient objects:

$$F(x) = \frac{[I(x)-\mu_{\rm in}]^2}{2\sigma_{\rm in}^2} - \frac{[I(x)-\mu_{\rm out}]^2}{2\sigma_{\rm out}^2} + \text{Log}\left(\frac{\sigma_{\rm out}}{\sigma_{\rm in}}\right). \quad \text{(A2)}$$

Here, F is the active contour energy, I is the image of interest, x is a point along the evolving contour and the rest of the nomenclature is the same as in equation (A1).

Experiments have suggested that the choice of the weighting parameter as well as the quality of the underlying data and the initial kernel size used to probe texture have little effect on the end segmentation result (see Fig. A4). We calculated the Dice values, which are a measure of how well automatically generated segmentations overlap with ground truths. For the results within Fig. A4, Dice values vary within a fairly decent range of 0.55 (in the extreme noise case) to 0.84.

A3 Magnetostatic forces

The sole reliance on either localized or magnetostatic forces to bring about acceptable segmentations is limiting, and this is evident from Fig. A5. In this figure, a comparison is made against the use of just magnetostatic information for segmentation against its combination with local image statistics. It can be seen that this complementary methodology can aid the image segmentation process. It is also preferable to just using local information, as the whole process would then be reliant upon the statistical approximation being made.

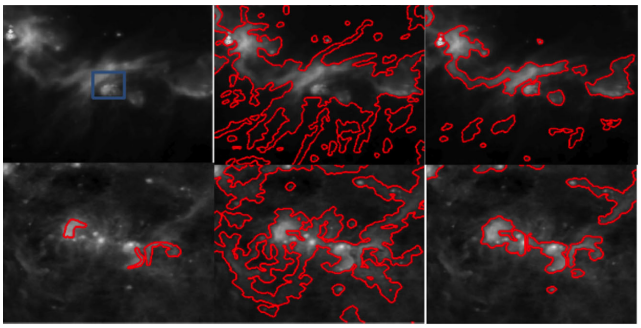

Figure A5. The improved results achieved when adaptive local active contours are used with magnetostatic forces. The first column is the original data, with examples of objects of interest highlighted by blue boxes/red outlines, the middle column is the magnetostatic forces by themselves and the last column is the result of the adaptive localized contour.

Magnetostatic forces are derived via a magnetic density flux coefficient matrix, $\boldsymbol{B}$, which is given by

$$e1 = g\cdot(-\nabla y\otimes)\frac{1}{r^2}; \qquad e2 = g\cdot\nabla x\otimes\frac{1}{r^2}$$
$$\boldsymbol{B} = \nabla e2 - \nabla e1, \quad \text{(A3)}$$

where $\otimes$ is the convolution operation performed in the frequency domain, g is the gradient magnitude of the image and r^2 is a centred Euclidean distance matrix padded to the maximum length of an image of interest for frequency filtering. Magnetostatic forces operate by creating a signed map of where regions of gradient reside in an image and the simple thresholding of this at zero, or another user-defined constant, produces a mask that can constrain the growth of the contour around areas of high gradient. This negates the use of background areas in the statistical analysis step of the segmentation.

The refinement of the segmentation with magnetostatic field diffusion and local image statistics has enabled an image segmentation pipeline that requires little human intervention. Intervention in this paper took the form of experimenting with different active contour energies and testing different kernel selection schemes. There is unlikely ever to be one active contour method that would be suitable for all astronomy data and an investigation of this sort should always be conducted before any attempt at the use of active contours is made. However, currently the segmentation just provides outlines of astronomical objects and makes no discrimination between the features it finds. Therefore, in the future, approaches will be developed that will allow machine-learning techniques to be utilized in the identification of objects of interest (e.g. bubbles).

Downloaded from https://academic.oup.com/mnras/article-abstract/473/3/3671/4633601
by guest
on 13 March 2018

APPENDIX B: PHOTOMETRY TABLES

Table B1. Golden sample aperture photometry at 12 and 22 μm (*WISE*).

Bubble ID	Long[a] (deg)	Lat[a] (deg)	R_{cat} [b] (arcsec)	12 μm Flux (Jy)	12 μm Err (Jy)	12 μm S/N	22 μm Flux (Jy)	22 μm Err (Jy)	22 μm S/N
MWP1G358760-007700S	358.760	−0.77	21.6	0.72	0.01	3.1	2.01	0.06	4.6
MWP1G358770+001090	358.770	0.109	20.2	0.25	0.01	5.3	1.00	0.06	4.4
MWP1G358840-007400S	358.840	−0.74	27.0	2.27	0.01	5.3	6.66	0.07	22.1
MWP1G358881+000576	358.881	0.058	40.0	18.02	0.02	33.5	52.88	0.13	27.2
MWP1G358890+000800S	358.890	0.08	20.4	1.15	0.01	8.5	2.81	0.06	9.2
MWP1G358950-000200S	358.950	−0.02	25.2	1.31	0.01	4.1	3.44	0.10	1.7
MWP1G359275-000403	359.275	−0.04	23.5	1.99	0.03	1.9	12.69	0.13	2.8
MWP1G359282-008955	359.282	−0.895	83.0	7.78	0.06	0.4	7.33	0.21	0.3
MWP1G359300+002883	359.300	0.288	195.7	55.49	0.14	0.3	162.05	0.56	0.3
MWP1G359350-004141	359.350	−0.414	49.5	2.68	0.03	1.9	34.60	0.14	7.3
MWP1G359411+000363	359.411	0.036	42.6	10.31	0.07	1.9	60.63	0.19	5.4
MWP1G359420+000200S	359.420	0.02	19.2	1.76	0.03	0.4	12.47	0.15	1.4
MWP1G359450-000200S	359.450	−0.02	24.0	0.23	0.02	0.2	7.63	0.12	1.5
MWP1G359514+002727	359.514	0.273	166.0	16.87	0.12	0.2	198.83	0.51	1.8
MWP1G359569-004772	359.569	−0.477	199.0	–	–	–	–	–	–
MWP1G359740-005900S	359.740	−0.59	22.8	1.62	0.01	6.8	7.16	0.06	34.8
⋮									

Notes. [a]Bubble Galactic coordinates given by Simpson et al. (2012).
[b]R_{cat} is taken from the catalogue of Simpson et al. (2012) and corresponds to the effective radius for small bubbles or to half the outer diameter for large bubbles.

Table B2. Golden sample segmentation photometry at 12 and 22 μm (*WISE*).

Bubble ID	Long[a] (deg)	Lat[a] (deg)	R_{cat} [b] (arcsec)	12 μm Flux (Jy)	12 μm Err (Jy)	12 μm S/N	22 μm Flux (Jy)	22 μm Err (Jy)	22 μm S/N
MWP1G358760–007700S	358.760	−0.77	21.6	0.85	0.01	4.0	2.25	0.06	5.7
MWP1G358770+001090	358.770	0.109	20.2	–	–	–	–	–	–
MWP1G358840–007400S	358.840	−0.74	27.0	2.41	0.01	6.3	6.62	0.06	21.5
MWP1G358881+000576	358.881	0.058	40.0	17.10	0.02	23.9	49.11	0.10	23.0
MWP1G358890+000800S	358.890	0.08	20.4	0.91	0.01	4.4	1.80	0.04	4.0
MWP1G358950–000200S	358.950	−0.02	25.2	1.27	0.01	3.2	4.60	0.07	3.0
MWP1G359275–000403	359.275	−0.04	23.5	–	–	–	–	–	–
MWP1G359282–008955	359.282	−0.895	83.0	–	–	–	–	–	–
MWP1G359300+002883	359.300	0.288	195.7	–	–	–	–	–	–
MWP1G359350–004141	359.350	−0.414	49.5	2.34	0.01	1.5	7.57	0.06	3.3
MWP1G359411+000363	359.411	0.036	42.6	–	–	–	–	–	–
MWP1G359420+000200S	359.420	0.02	19.2	–	–	–	–	–	–
MWP1G359450–000200S	359.450	−0.02	24.0	–	–	–	–	–	–
MWP1G359514+002727	359.514	0.273	166.0	–	–	–	–	–	–
MWP1G359569–004772	359.569	−0.477	199.0	–	–	–	–	–	–
MWP1G359740–005900S	359.740	−0.59	22.8	1.48	0.01	4.3	6.78	0.05	23.9
⋮									

Notes. [a]Bubble Galactic coordinates given by Simpson et al. (2012).
[b]R_{cat} is taken from the catalogue by Simpson et al. (2012) and corresponds to the effective radius for small bubbles or to half the outer diameter for large bubbles.

Downloaded from https://academic.oup.com/mnras/article-abstract/473/3/3671/4633601
by guest
on 13 March 2018

Table B3. Golden sample aperture and segmentation photometry at 70 μm (*Herschel*).

Bubble ID	Long[a] (deg)	Lat[a] (deg)	R_{cat} [b] (arcsec)	Aperture photometry			Segmentation photometry		
				Flux (Jy)	Err (Jy)	S/N	Flux (Jy)	Err (Jy)	S/N
MWP1G358760–007700S	358.760	– 0.77	21.6	47.20	0.68	6.3	47.15	0.22	10.0
MWP1G358770+001090	358.770	0.109	20.2	23.39	1.15	3.5	–	–	–
MWP1G358840–007400S	358.840	– 0.74	27.0	166.08	0.99	20.5	165.75	0.41	19.8
MWP1G358881+000576	358.881	0.058	40.0	1103.74	6.95	11.4	1102.47	2.34	12.1
MWP1G358890+000800S	358.890	0.08	20.4	98.44	1.88	6.7	85.73	0.63	5.6
MWP1G358950–000200S	358.950	– 0.02	25.2	57.45	5.42	0.8	131.68	1.00	4.1
MWP1G359275–000403	359.275	– 0.04	23.5	243.59	5.40	3.2	–	–	–
MWP1G359282–008955	359.282	– 0.895	83.0	181.10	4.89	0.1	–	–	–
MWP1G359300+002883	359.300	0.288	195.7	2875.17	22.17	0.2	–	–	–
MWP1G359350–004141	359.350	– 0.414	49.5	12.27	3.31	0.5	59.75	0.53	0.3
MWP1G359411+000363	359.411	0.036	42.6	1262.36	9.62	3.6	–	–	–
MWP1G359420+000200S	359.420	0.02	19.2	411.34	6.92	2.8	–	–	–
MWP1G359450–000200S	359.450	– 0.02	24.0	***	***	***	–	–	–
MWP1G359514+002727	359.514	0.273	166.0	3960.82	12.21	1.9	–	–	–
MWP1G359569–004772	359.569	– 0.477	199.0	8392.94	18.38	1.6	–	–	–
MWP1G359740–005900S	359.740	– 0.59	22.8	111.24	0.97	9.6	109.41	0.37	11.5
⋮									

Notes. [a]Bubble Galactic coordinates given by Simpson et al. (2012).
[b]R_{cat} is taken from the catalogue of Simpson et al. (2012) and corresponds to the effective radius for small bubbles or to half the outer diameter for large bubbles.

Table B4. Golden sample aperture and segmentation photometry at 160 μm (*Herschel*).

Bubble ID	Long[a] (deg)	Lat[a] (deg)	R_{cat} [b] (arcsec)	Aperture photometry			Segmentation photometry		
				Flux (Jy)	Err (Jy)	S/N	Flux (Jy)	Err (Jy)	S/N
MWP1G358760–007700S	358.760	– 0.77	21.6	128.25	2.22	9.8	235.62	3.00	1.9
MWP1G358770+001090	358.770	0.109	20.2	31.23	6.15	0.7	–	–	–
MWP1G358840–007400S	358.840	– 0.74	27.0	289.98	3.48	11.1	280.10	2.80	3.3
MWP1G358881+000576	358.881	0.058	40.0	789.43	12.56	5.9	527.76	8.96	2.1
MWP1G358890+000800S	358.890	0.08	20.4	148.42	6.62	3.2	***	***	***
MWP1G358950–000200S	358.950	– 0.02	25.2	44.45	7.86	1.3	452.10	9.99	1.4
MWP1G359275–000403	359.275	– 0.04	23.5	155.56	14.64	0.6	–	–	–
MWP1G359282–008955	359.282	– 0.895	83.0	561.47	15.14	0.3	–	–	–
MWP1G359300+002883	359.300	0.288	195.7	7833.53	51.46	0.9	–	–	–
MWP1G359350–004141	359.350	– 0.414	49.5	70.59	8.79	0.9	***	***	***
MWP1G359411+000363	359.411	0.036	42.6	973.32	15.11	2.0	–	–	–
MWP1G359420+000200S	359.420	0.02	19.2	345.95	13.36	2.2	–	–	–
MWP1G359450–000200S	359.450	– 0.02	24.0	– 267.39	15.42	– 1.4	–	–	–
MWP1G359514+002727	359.514	0.273	166.0	3574.36	46.98	0.4	–	–	–
MWP1G359569–004772	359.569	– 0.477	199.0	8238.16	72.53	0.4	–	–	–
MWP1G359740–005900S	359.740	– 0.59	22.8	104.36	1.88	10.7	14.05	0.52	8.8
⋮									

Notes. [a]Bubble Galactic coordinates given by Simpson et al. (2012).
[b]R_{cat} is taken from the catalogue of Simpson et al. (2012) and corresponds to the effective radius for small bubbles or to half the outer diameter for large bubbles.

Downloaded from https://academic.oup.com/mnras/article-abstract/473/3/3671/4633601
by guest
on 13 March 2018

Table B5. Golden sample aperture and segmentation photometry at 250 μm (*Herschel*).

Bubble ID	Long[a] (deg)	Lat[a] (deg)	R_{cat} [b] (arcsec)	Aperture photometry			Segmentation photometry		
				Flux (Jy)	Err (Jy)	S/N	Flux (Jy)	Err (Jy)	S/N
MWP1G358760–007700S	358.760	−0.77	21.6	89.05	1.74	7.3	158.04	1.91	2.0
MWP1G358770+001090	358.770	0.109	20.2	17.52	4.58	0.5	–	–	–
MWP1G358840–007400S	358.840	−0.74	27.0	179.74	2.82	8.7	107.62	0.63	9.3
MWP1G358881+000576	358.881	0.058	40.0	372.57	7.56	4.5	***	***	***
MWP1G358890+000800S	358.890	0.08	20.4	84.45	5.64	2.1	***	***	***
MWP1G358950–000200S	358.950	−0.02	25.2	41.75	4.26	2.3	168.01	5.60	1.5
MWP1G359275–000403	359.275	−0.04	23.5	59.48	11.92	0.4	–	–	–
MWP1G359282–008955	359.282	−0.895	83.0	292.88	9.32	0.3	–	–	–
MWP1G359300+002883	359.300	0.288	195.7	4420.15	30.40	1.4	–	–	–
MWP1G359350–004141	359.350	−0.414	49.5	84.00	5.12	1.4	***	***	***
MWP1G359411+000363	359.411	0.036	42.6	256.28	9.06	0.3	–	–	–
MWP1G359420+000200S	359.420	0.02	19.2	88.14	10.27	0.9	–	–	–
MWP1G359450–000200S	359.450	−0.02	24.0	***	***	***	–	–	–
MWP1G359514+002727	359.514	0.273	166.0	564.90	36.44	−0.1	–	–	–
MWP1G359569–004772	359.569	−0.477	199.0	1229.62	55.34	−0.0	–	–	–
MWP1G359740–005900S	359.740	−0.59	22.8	–	–	–	–	–	–
⋮									

Notes. [a]Bubble Galactic coordinates given by Simpson et al. (2012).
[b]R_{cat} is taken from the catalogue of Simpson et al. (2012) and corresponds to the effective radius for small bubbles or to half the outer diameter for large bubbles.

Table B6. Golden sample aperture and segmentation photometry at 350 μm (*Herschel*).

Bubble ID	Long[a] (deg)	Lat[a] (deg)	R_{cat} [b] (arcsec)	Aperture photometry			Segmentation photometry		
				Flux (Jy)	Err (Jy)	S/N	Flux (Jy)	Err (Jy)	S/N
MWP1G358760–007700S	358.760	−0.77	21.6	49.06	1.13	7.7	72.29	0.86	2.3
MWP1G358770+001090	358.770	0.109	20.2	4.65	2.57	0.6	–	–	–
MWP1G358840–007400S	358.840	−0.74	27.0	87.14	1.86	8.1	40.84	0.32	9.2
MWP1G358881+000576	358.881	0.058	40.0	170.20	4.10	4.5	***	***	***
MWP1G358890+000800S	358.890	0.08	20.4	29.93	4.48	1.4	***	***	***
MWP1G358950–000200S	358.950	−0.02	25.2	22.82	2.45	2.8	67.34	2.39	1.5
MWP1G359275–000403	359.275	−0.04	23.5	29.32	7.17	0.4	–	–	–
MWP1G359282–008955	359.282	−0.895	83.0	116.16	4.97	0.3	–	–	–
MWP1G359300+002883	359.300	0.288	195.7	1995.04	16.34	1.6	–	–	–
MWP1G359350–004141	359.350	−0.414	49.5	52.52	2.73	2.0	***	***	***
MWP1G359411+000363	359.411	0.036	42.6	59.42	5.07	−0.6	–	–	–
MWP1G359420+000200S	359.420	0.02	19.2	41.18	5.30	1.1	–	–	–
MWP1G359450–000200S	359.450	−0.02	24.0	***	***	***	–	–	–
MWP1G359514+002727	359.514	0.273	166.0	116.42	20.75	−0.2	–	–	–
MWP1G359569–004772	359.569	−0.477	199.0	242.08	30.33	−0.1	–	–	–
MWP1G359740–005900S	359.740	−0.59	22.8	–	–	–	–	–	–
⋮									

Notes. [a]Bubble Galactic coordinates given by Simpson et al. (2012).
[b]R_{cat} is taken from the catalogue of Simpson et al. (2012) and corresponds to the effective radius for small bubbles or to half the outer diameter for large bubbles.

Downloaded from https://academic.oup.com/mnras/article-abstract/473/3/3671/4633601
by guest
on 13 March 2018

Table B7. Golden sample aperture and segmentation photometry at 500 μm (*Herschel*).

Bubble ID	Long[a] (deg)	Lat[a] (deg)	R_{cat} [b] (arcsec)	Aperture photometry			Segmentation photometry		
				Flux (Jy)	Err (Jy)	S/N	Flux (Jy)	Err (Jy)	S/N
MWP1G358760–007700S	358.760	−0.77	21.6	18.37	0.62	7.1	21.47	0.32	2.2
MWP1G358770+001090	358.770	0.109	20.2	4.03	1.16	0.7	–	–	–
MWP1G358840–007400S	358.840	−0.74	27.0	31.63	0.96	9.0	4.80	0.12	7.8
MWP1G358881+000576	358.881	0.058	40.0	59.86	1.91	4.5	***	***	***
MWP1G358890+000800S	358.890	0.08	20.4	13.25	2.67	0.9	***	***	***
MWP1G358950–000200S	358.950	−0.02	25.2	13.90	1.23	3.7	22.26	0.81	1.6
MWP1G359275–000403	359.275	−0.04	23.5	16.79	3.54	0.4	–	–	–
MWP1G359282–008955	359.282	−0.895	83.0	40.35	2.21	0.4	–	–	–
MWP1G359300+002883	359.300	0.288	195.7	660.95	7.46	1.6	–	–	–
MWP1G359350–004141	359.350	−0.414	49.5	21.17	1.32	2.3	***	***	***
MWP1G359411+000363	359.411	0.036	42.6	11.02	2.50	−0.7	–	–	–
MWP1G359420+000200S	359.420	0.02	19.2	20.67	2.27	1.4	–	–	–
MWP1G359450–000200S	359.450	−0.02	24.0	***	***	***	–	–	–
MWP1G359514+002727	359.514	0.273	166.0	45.81	9.36	−0.2	–	–	–
MWP1G359569–004772	359.569	−0.477	199.0	42.60	13.86	−0.2	–	–	–
MWP1G359740–005900S	359.740	−0.59	22.8	–	–	–	–	–	–
⋮									

Notes. [a]Bubble Galactic coordinates given by Simpson et al. (2012).
[b]R_{cat} is taken from the catalogue of Simpson et al. (2012) and corresponds to the effective radius for small bubbles or to half the outer diameter for large bubbles.

This paper has been typeset from a TEX/LATEX file prepared by the author.

Downloaded from https://academic.oup.com/mnras/article-abstract/473/3/3671/4633601
by guest
on 13 March 2018